Profile catalogue for airfoil sections based on 3D computations

Bertagnolio, Franck; Sørensen, Niels N.; Johansen, Jeppe

Publication date:
2006

Document Version
Publisher's PDF, also known as Version of record

Risø-R-1581(EN)

Profile Catalogue for Airfoil Sections Based on 3D Computations

Franck Bertagnolio, Niels N. Sørensen and Jeppe Johansen

Risø National Laboratory
Roskilde
Denmark
December 2006

Author: Franck Bertagnolio, Niels N. Sørensen and Jeppe Johansen
Title: Profile Catalogue for Airfoil Sections Based on 3D Computations
Department: Wind Energy Department

Abstract (max. 2000 char.):
This report is a continuation of the Wind Turbine Airfoil Catalogue [1] which objective was, firstly to provide a database of aerodynamic characteristics for a wide range of airfoil profiles aimed at wind turbine applications, and secondly to test the two-dimensional Navier-Stokes solver EllipSys2D by comparing its results with experimental data. In the present work, the original two-dimensional results are compared with three-dimensional calculations as it was surmised that the two-dimensional assumption might be in some cases responsible for discrepancies between the numerical flow solution and the actual fluid flow, and thereby the incorrect prediction of airfoil characteristics. In addition, other features of the flow solver, such as transition and turbulence modelling, and their influence onto the numerical results are investigated. Conclusions are drawn regarding the evaluation of airfoil aerodynamic characteristics, as well as the use of the Navier-Stokes solver for fluid flow calculations in general.

Risø-R-1581(EN)
December 2006

ISSN 0106-2840
ISBN 87-550-3563-9

Contract no.:
ENS-33031-0077

Group's own reg. no.:
1110047-01

Sponsorship:
Danish Energy Authority

Cover :

Pages: 72
Tables: 0
References: 24

Risø National Laboratory
Information Service Department
P.O.Box 49
DK-4000 Roskilde
Denmark
Telephone +45 46774004
bibl@risoe.dk
Fax +45 46774013
www.risoe.dk

Risø–R–1581(EN)

Profile Catalogue for Airfoil Sections Based on 3D Computations

Franck Bertagnolio, Niels N. Sørensen and Jeppe Johansen

Risø National Laboratory, Roskilde, Denmark
December 2006

Abstract This report is a continuation of the Wind Turbine Airfoil Catalogue [1] which objective was, firstly to provide a database of aerodynamic characteristics for a wide range of airfoil profiles aimed at wind turbine applications, and secondly to test the two-dimensional Navier-Stokes solver EllipSys2D by comparing its results with experimental data. In the present work, the original two-dimensional results are compared with three-dimensional calculations as it was surmised that the two-dimensional assumption might be in some cases responsible for discrepancies between the numerical flow solution and the actual fluid flow, and thereby the incorrect prediction of airfoil characteristics. In addition, other features of the flow solver, such as transition and turbulence modelling, and their influence onto the numerical results are investigated. Conclusions are drawn regarding the evaluation of airfoil aerodynamic characteristics, as well as the use of the Navier-Stokes solver for fluid flow calculations in general.

ISBN 87–550–3563–9 (Internet)
ISSN ????–????

Print: Pitney Bowes Management Services Denmark A/S · 2006

Contents

1 Introduction

After the publication of the Wind Turbine Airfoil Catalogue [1] which presented two-dimensional computational results for a wide range of wind turbine airfoils, and compared these results with experimental data when available, it was surmised that some discrepancies might originate from the two-dimensional approximation. It was therefore suggested that an investigation of the three-dimensional effects on the prediction of airfoil characteristics using Navier-Stokes computations should be undertaken.

The aim of this work is to evaluate the prediction capabilities of the computational code EllipSys3D compared to its two-dimensional version EllipSys2D on one side, and the experimental results (when available) on the other side. In order to perform this study, the flow around three-dimensional blade sections for chosen airfoil profiles will be computed. Several aspects of the numerical code are investigated. A numerical parameter dependency analysis is performed at the beginning of the study in order to ensure the reliability of the computational results. As it was clearly shown in the Wind Turbine Airfoil Catalogue [1], transition modelling is a decisive factor for airfoil characteristics prediction. Therefore, the influence of the implementation of (simplified) three-dimensional transition models will be investigated. In addition, turbulence modelling in the form of Reynolds-Averaged Navier-Stokes equations and of the Detached Eddy Simulation model, as well as their influence on characteristics prediction, are studied.

It is well-known that the numerical solution of the three-dimensional Navier-Stokes equations is computationally very demanding. It is therefore not possible to deal with as many airfoil profiles as it was done in the Wind Turbine Airfoil Catalogue which involved only 2D calculations. Instead it is decided to concentrate on a few chosen airfoils (namely the 4 following profiles: RISØ-B1-18, NACA 63-430, S809 and DU 83-W-210), and perform more specific calculations in order to highlight what can be gained from three-dimensional computations compared to two-dimensional ones, as well as clarify some numerical and modelling issues. The above-mentioned airfoils were chosen as they have aerodynamic behaviors quite different from each other, and are therefore assumed to be representative for a wide range of wind turbine airfoils.

The text is organised as follows. After describing our numerical model, a preliminary study is performed in order to investigate the influence of several numerical parameters on the results. Thereafter, the 4 different airfoils that were found relevant for this study are computed. Finally, the results are analyzed and it is attempted to draw some general conclusions.

2 Navier-Stokes Solver

In this section, the Navier-Stokes solver that is used to perform the aerodynamic calculations presented in this study is introduced. Thereafter, the mesh generation strategy is described.

2.1 Numerical Method

The fluid flow solver EllipSys3D (and its two-dimensional version EllipSys2D) is an in-house code which was developed in a co-operation between the Department of Mechanical Engineering at DTU (Technical University of Denmark) and the Department of Wind Energy at Risø National Laboratory. A detailed description of the numerical code can be found in the references [14, 15, 17].

This code is designed to solve the three-dimensional Navier-Stokes equations for an incompressible fluid. It uses a cell-centered grid arrangement for the pressure field and the cartesian velocity components. The equations are discretised by means of a finite volume formulation. The well-known velocity-pressure decoupling is circumvented by using the Rhie and Chow interpolation technique [16]. For unsteady computations, the PISO algorithm is used for solving the momentum and pressure equations in a predictor-corrector fashion [8].

Various schemes for the discretisation of the convective terms are implemented. In this study, the third order accurate QUICK upwind scheme by Leonard [11] was used for all simulations. However, for calculations using the Detached Eddy Simulation model (see below), a fourth order accurate central difference scheme was used where the Large Eddy Simulation model is effective in order to more accurately simulate the dynamics of the larger flow structures. The viscous terms are discretised with the classical second order central difference scheme. A subiteration technique is implemented in order to increase the critical time-step.

The fluid flows that are studied in this report are characterized by high Reynolds numbers. Therefore, a turbulence model must be implemented in the flow solver. In our case, the $k-\omega$ SST turbulence model by Menter [12] in its original version was used to obtain the turbulent viscosity. Calculations using uniquely this model are referred as Reynolds-Averaged Navier-Stokes (RANS) computations, both in 2D and 3D. In the case of three-dimensional simulations, a Detached Eddy Simulation (DES) technique [21, 22] was also implemented as described in [9, 10]. This model uses the above-mentioned $k-\omega$ SST model in the vicinity of the airfoil, avoiding the need for highly refined grid cells in this region of the flow, whereas a Large Eddy Simulation (LES) model, namely a Smagorinsky-like model [19], is used in the far field. LES models fully simulate the unsteady dynamics of the larger scales of the flow, whereas the smaller eddies which cannot be captured by the computational grid (also referred as subgrid scales) are modelled by an algebraic turbulent eddy viscosity class model.

The numerical code requires that the computational domain must be mapped onto a boundary-fitted structured grid. In order to facilitate the mapping and to take advantage of the new generation of parallel computers, a domain decomposition technique has been implemented. The meshes of the individual subdomains must be conformal, i.e. the grid lines must match at the interfaces between the subdomains. In a parallel computing platform, each processor is handling a certain number of subdomains. The communications between the processors are performed by using the MPI-library.

2.2 Transition Modelling

It is well-known that transition to turbulence of the boundary layer can have a great impact on airfoil aerodynamic performance. In some of our calculations, the flow was assumed to be fully turbulent. Two simplified transition models were also implemented.

The first model is a trivial one, where the transition location on the suction and the pressure side of the airfoil were simply fixed at a constant chord location (different on each side) along the whole span of the airfoil. These locations were either extracted from experimental measurements in one case, or from two-dimensional calculations of an identical airfoil profile using EllipSys2D for which the transition model by Drela [4] was implemented as described in [13]. It will be referred as *fixed transition model* in this report.

A second model also originating from two-dimensional calculations was implemented [18]. The transition locations on both sides of the airfoil were beforehand extracted from 2D computations together with the stagnation point location. This is done for the whole range of angles of attack that are considered in the study. During a 3D calculation, the stagnation point location is determined at some predefined stations along the airfoil span. The transition locations at these specific stations are then interpolated from the above-mentioned extracted data. In our case, this procedure is applied at 16 stations along the span of the airfoil, which will be set equal to 3 chord lengths in our calculations (see mesh generation in section 2.4). Between these predefined stations, transition locations are linearly interpolated. This model will be referred in the report as *simplified transition model*.

2.3 Boundary Conditions

As it is the normal procedure for a Navier-Stokes solver, no-slip boundary conditions are enforced at the airfoil surface. The outer boundary surface is divided into two parts. The first one is the inflow boundary for which the velocity at infinity is enforced. The second one is the outflow boundary for which homogeneous Neumann boundary conditions are prescribed.

It was checked that the whole computational domain was large enough (i.e. the distance from the airfoil to the outer boundary, see next section) so that the outer boundary conditions do not interfere with the flow, and thereby the aerodynamic forces, over the airfoil.

In the spanwise direction, periodic boundary conditions are enforced at the two extremities of the domain. Even if this configuration is not fully identical to actual experiments (for which there usually exist solid walls at each end of the airfoil section to prevent the occurrence of three-dimensional effects), it is assumed that the middle section of the experimental setup where the measurements are performed will be free of the influence of the walls, and therefore computational and experimental results can be compared.

2.4 Mesh Generation

In all our computations, the computational meshes have the following characteristics. These are O-type meshes extending approximately up to 35 chord lengths away from the airfoil. The grid generation is such that the cells are roughly square from 1/10 of the chord length away from the airfoil up to one chord length (see pictures of the reference grid defined below in Fig. 1). This last particular feature is preferable for the DES computations that will be performed in this study. Indeed, the use of a LES model (which is quite probable in this area of the flow field)

requires that the cells are approximately square in order to ensure its accuracy.

Our reference grid involves 256 cells around the airfoil surface and 256 in the direction perpendicular to the airfoil surface. The heigth of the first cell on the airfoil is $1{\times}10^{-7}$ (non-dimensionalised with respect to the chord length), leading in all cases to a $y^+ < 1$ for the first cell heigth (y^+ being the usual non-dimensional wall distance for turbulent boundary layer defined as $y^+ = \rho\, u_\tau y/\mu$, u_τ is the friction velocity). The grid is stretched toward both the trailing and the leading edge of the airfoil (see Fig. 1(c)).

The grids used for all 3D computations in this study are based on the grids that have just been defined above for the 2D computations. It is simply generated by lining up the same 2D grid in the spanwise direction. The cell size in the spanwise direction, i.e. the distance between two identical two-dimensional grids next to each other along the airfoil span, is equal to 1.56×10^{-2}, and there are 192 cells in that direction. Consequently, the total mesh extends over a length of 3.0 airfoil chords in the spanwise direction, and results in approximately 12.6×10^6 cells.

The aboved-described mesh will be referred as the finest mesh M1 in the mesh refinement dependency analysis performed in the next section.

Note that all results that will be displayed in the figures of this report involve dimensionless quantities (except for angles of attack that will be measured in degrees). The reference quantities used for non-dimensionalisation will always be the airfoil chord length, the inflow velocity, and the air density and viscosity.

The angle of attack will be often referred to as the quantity α. It will always be the geometrical angle of attack in the case of Navier-Stokes computations. As for the measurements, corrections are usually applied to the measured geometrical angle of attack accounting for wind tunnel effects. The corrected angles are always given.

It should also be noted that the skin friction coefficient calculated in all 3D computations will always be displayed as a positive value. This is due to the difficulty to define the orientation of the flow on a 2D surface. For 2D computations, a negative skin friction will still mean a reverse flow and thereby a recirculation bubble or a detached region. The pressure coefficient is defined as usual for airfoil applications as:

$$Cp = -\frac{p - p_\infty}{2\,\rho\, U_\infty^2\, C}$$

where p_∞ and U_∞ denotes respectively the pressure and velocity at infinity, ρ is the density of the fluid, and C the chord of the profile. As a consequence, when a high pressure coefficient will be mentioned in the following text, this will in fact mean a low pressure or suction. Conversely, a low pressure coefficient will mean a high pressure.

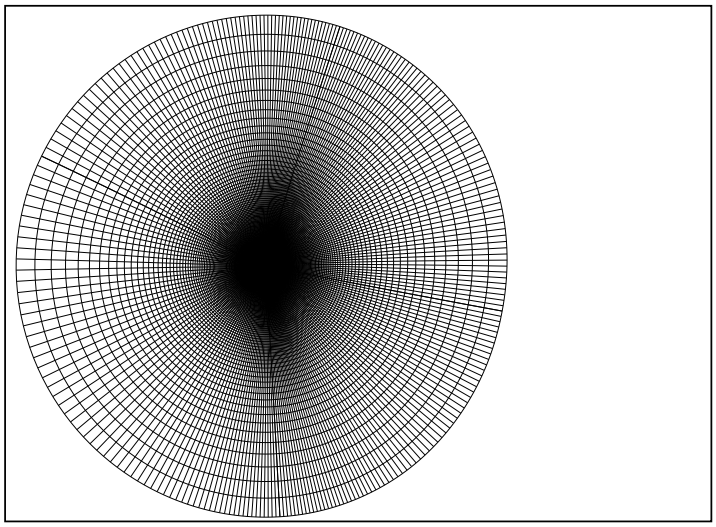

(a) Extended View

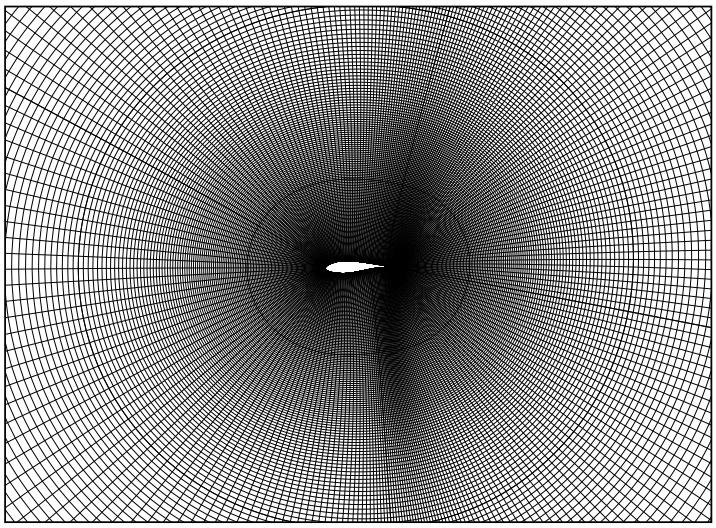

(b) Close-up 1

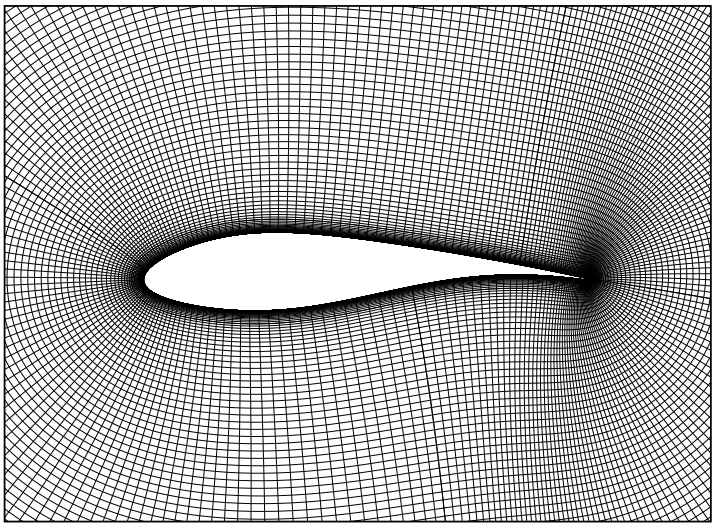

(c) Close-up 2

Figure 1. Computational Grid for the RISØ-B1-18 Airfoil

3 Numerical Parameter Analysis

As a starting point for our study, a numerical parameter analysis is performed. The influence of the mesh refinement, the time-step, and the span width of the airfoil are studied. Three-dimensional simulations of the flow around the RISØ-B1-18 airfoil are performed with the Navier-Stokes solver at an angle of attack set to 18^o. Calculations are performed with the DES model. The influence of turbulence and transition modelling will be considered further in this work.

3.1 Mesh Refinement Analysis

The influence of the mesh refinement is studied. The reference mesh defined in section 2.4 is referred as mesh M1. A second mesh is defined by retaining every second mesh vertex of the reference mesh in all directions, and is referred as mesh M2. A third mesh M3 is defined by only retaining every fourth mesh vertex of the reference mesh. The lift time-series are displayed in Figs. 2(a-b) for a span width of the airfoil equal to 2 and 3 chord lengths, respectively. Drag time-series are displayed in Figs. 2(c-d). The cell length in the spanwise direction is kept the same in both cases, and meshes are referred as M1 or M2 independently of the span width. The time-step is set to $\Delta t = 0.02$.

It can be seen that the results obtained with mesh M1 are almost converged as the discrepencies between the mean values of the results of meshes M1 and M2 are much smaller than between meshes M2 and M3. It is therefore decided that the finest mesh M1 will be used in the remaining of this study, as the number of cells involved with an even finer mesh would be prohibitive in terms of computational time. However, it is important here to clarify the concept of convergence with respect to mesh refinement for these kinds of computations. Indeed, as long as a DES model is used, a further refinement of the computational grid will contribute to the emergence of smaller structures that can be captured by the mesh. Therefore, the unsteady features of the computed flow will never converge as the mesh is refined (unless the mesh is so fine that the simulation reduces to a Direct Numerical Simulation for which the turbulence model is never active, and all turbulent structures are captured by the grid and simulated by the flow solver). Nevertheless, it is assumed that the DES model is reliable enough so that the results will converge (as numerical errors are progressively removed) toward numerical solutions which are converging in mean values as the mesh is refined.

3.2 Time-Step Dependency Analysis

The influence of the time-step used for the unsteady calculations is studied. Four different time-steps are used: $\Delta t = 0.04$, 0.02, 0.01 and 0.005. The span width of the airfoil is equal to 3 chord lengths. The time-series of lift and drag are respectively plotted on Figs. 3(a-b).

It can be seen that the largest time-step $\Delta t = 0.04$ is generating large numerical wiggles (see details on Figs. 3(c-d)). These wiggles can sporadically also be observed for the two shorter time-steps $\Delta t = 0.02$ and 0.01, but much more damped. The two shortest time-steps $\Delta t = 0.01$ and 0.005 give nearly similar results, and the intermediate time-step $\Delta t = 0.02$ predicts only slightly higher lift and drag. It was decided to use the later time-step in the remaining of this report for most of the computations. For particular airfoils (DU 93-W-210 and NACA 64-430) however, it produced the large numerical wiggles as observed for the previous largest time-step. Therefore, in these two cases a time-step equal to $\Delta t = 0.01$ was used.

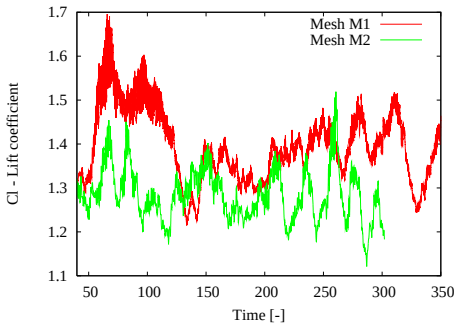

(a) Lift - Span=2

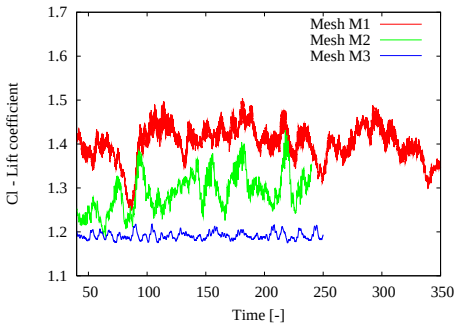

(b) Lift - Span=3

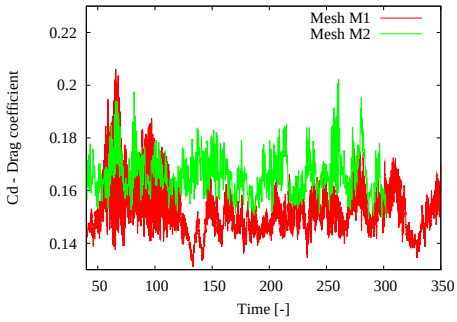

(c) Drag - Span=2

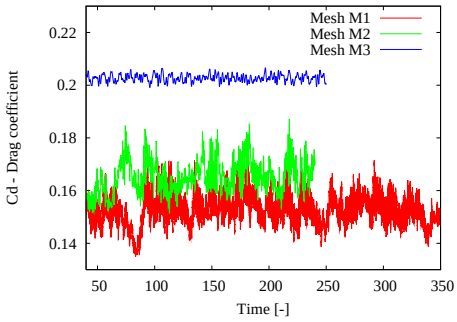

(d) Drag - Span=3

Figure 2. Mesh Refinement Analysis for RISØ-B1-18 Airfoil at $\alpha = 18^o$

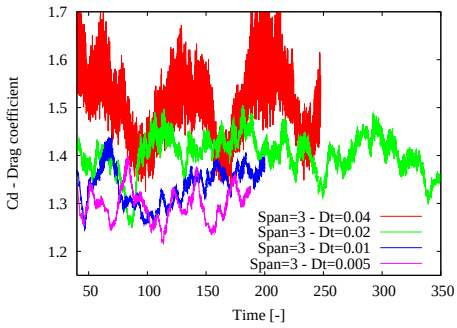

(a) Lift coefficient

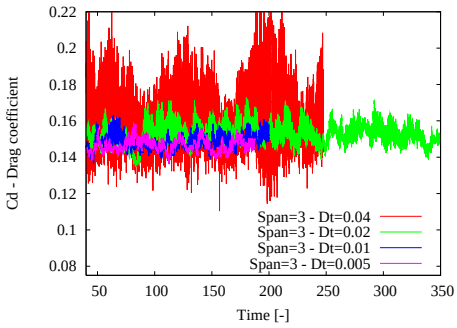

(b) Drag coefficient

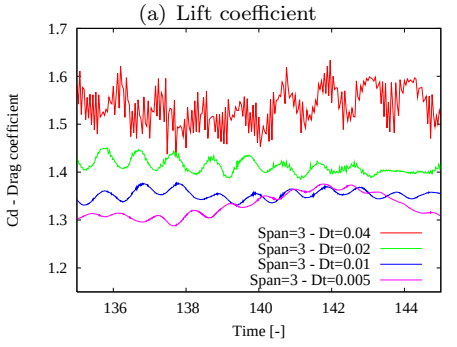

(c) Lift coefficient - Close-up

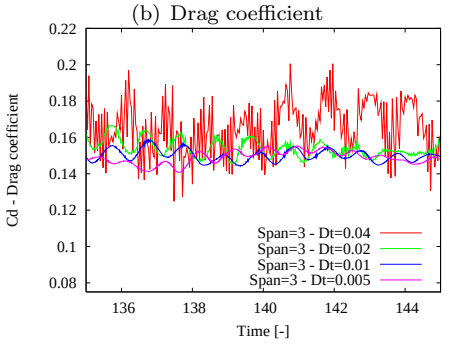

(d) Drag coefficient - Close-up

Figure 3. Time-Step Dependency Analysis for RISØ-B1-18 Airfoil at $\alpha = 18^o$

3.3 Span Width Dependency Analysis

The influence of the span width of the airfoil section is studied. Three different span widths are used: 2, 3 and 6 chord lengths. For all calculations the time-step

is set equal to $\Delta t = 0.02$. Lift time-series are plotted on Fig. 4(a) for the finer mesh M1, and Fig. 4(b) for the coarser mesh M2. As it can be seen, there is nearly no differences in the average characteristics for all span widths. In the remaining of this paper, a span width equal to 3 chord lengths will be used.

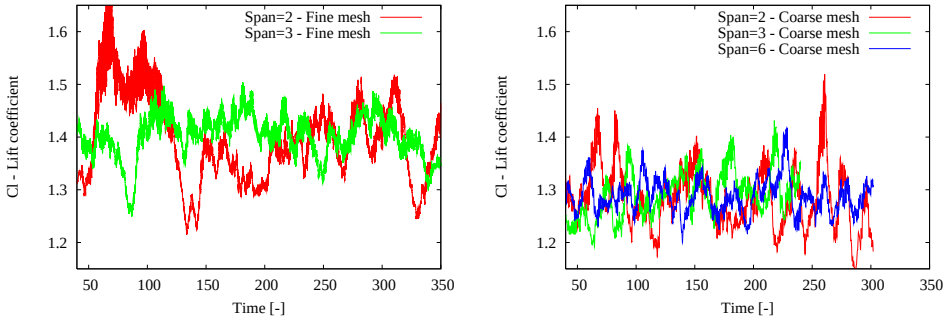

(a) Finer Mesh M1 (b) Coarser Mesh M2

Figure 4. Span Width Dependency Analysis for RISØ-B1-18 Airfoil at $\alpha = 18^o$

In order to appraise the forces distribution along the airfoil span, lift and drag time-series at different stations along the airfoil span are plotted on Figs. 5(a-b), respectively. Shorter time-series of the lift and drag are extracted and displayed on Figs. 5(c-d). Oscillations of period nearly equal to $T = 1$ can be observed at all stations along the airfoil span. Moreover, these oscillations are in phase between all stations indicating the occurrence of a 2D vortex shedding as it was observed in a previous study [3, 2].

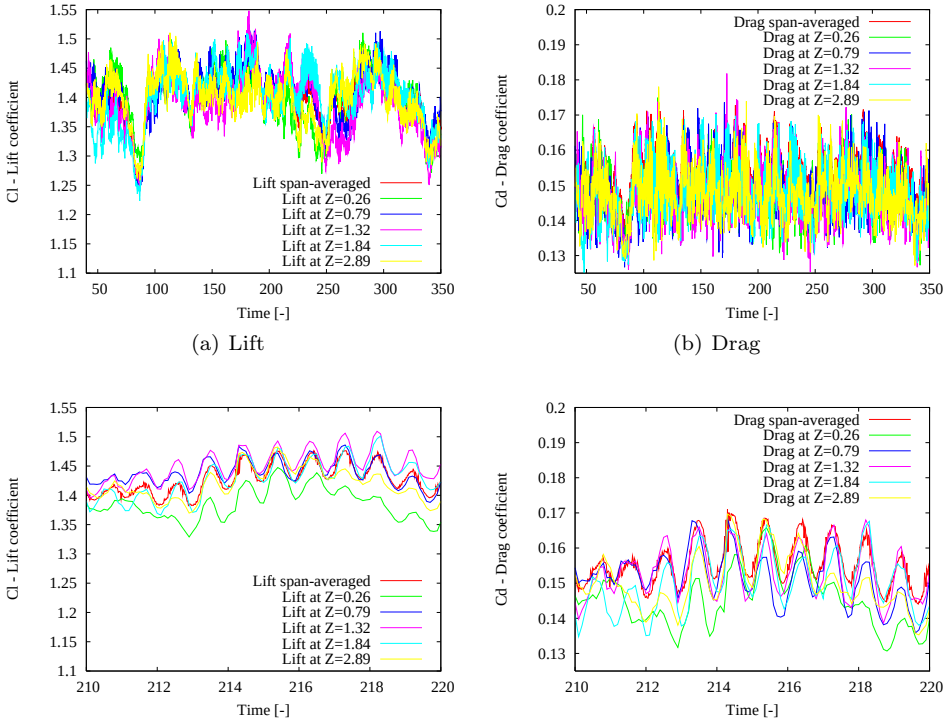

(a) Lift (b) Drag

(c) Lift - Close-up (d) Drag - Close-up

Figure 5. Forces Distribution along the Span for RISØ-B1-18 Airfoil at $\alpha = 18^o$

3.4 Turbulence and Transition Models Influence

As turbulence and transition modelling are considered to be more related to the physics of the flow than to actual numerical parameters, their influence will be investigated separately for each individual airfoil.

4 Results for the RISØ-B1-18 Airfoil

The RISØ-B1 airfoil family was developed and optimized at Risø National Laboratory for use on wind turbines. One of the design objectives of this airfoil family was insensitivity to transition location around maximum lift, or more precisely the design of the airfoil was done such that transition should always occur just downstream of the leading edge suction peak if this one fails to trigger transition. This was achieved by avoiding a pressure plateau (or inverse pressure gradient) in the vicinity of the leading edge on the suction side. Indeed, as it will be seen in this section, the results obtained with transition model are quite similar to those obtained in a fully turbulent configuration. The transition always occurs relatively close to the leading edge suction peak.

In this study, the 18% thick airfoil RISØ-B1-18 is studied. It was tested in the VELUX wind tunnel, which has an open test section with a background turbulence level of 1%. The testing facility is described in detail in Fuglsang *et al* [6]. Tests were performed at a Reynolds number equal to $Re = 1.6 \times 10^6$ (see [7] for more details on the measurements). The airfoil section test stand was such that the span width of the airfoil was 3.2 chord lenths, and end plates were fixed at the ends of the airfoil to limit 3D flow effects.

4.1 Test cases

The computations were performed with the DES turbulence model for the 3D calculations, and with the $k - \omega$ SST turbulence model for the 2D calculations (RANS computations), as well as for 3D computations for a few chosen angles of attack. In addition, the influence of the implementation of a transition model is studied. Fully turbulent configurations are performed, as well as computations with the fixed transition model. Transition locations were extracted from 2D calculations with the transition model by Drela [4] implemented as described in [13]. The time-step is set to $\Delta t = 0.02$.

4.2 Results

Lift and drag characteristics for all computations are gathered on Figs. 6(a-b). It can be observed that there is a good agreement between all numerical computations and the experimental results in the linear region up to $\alpha = 10^o$. The 2D and 3D RANS calculations predict a lift increase up to an angle of attack equal to 14^o as in the measurements. The 2D calculations predict a lift drop just after stall similar to the measurements. In contrast, 3D DES computations (both fully turbulent and with transition model) predict an earlier stall at $\alpha = 10^o$, and therefore a rather smooth stall lift drop. At higher angles of attack ($\alpha > 18^o$), the 2D computations exhibit a new increase of lift which is not present in the 3D computations and the experimental results.

Transition locations on both side of the airfoil as a function of the angle of attack that were computed in the 2D RANS calculations with the transition model by Drela [4] are plotted on Fig. 7.

In the following of this section, 2D and 3D computations are compared. The influence of the turbulence model and of the implementation of transition are investigated.

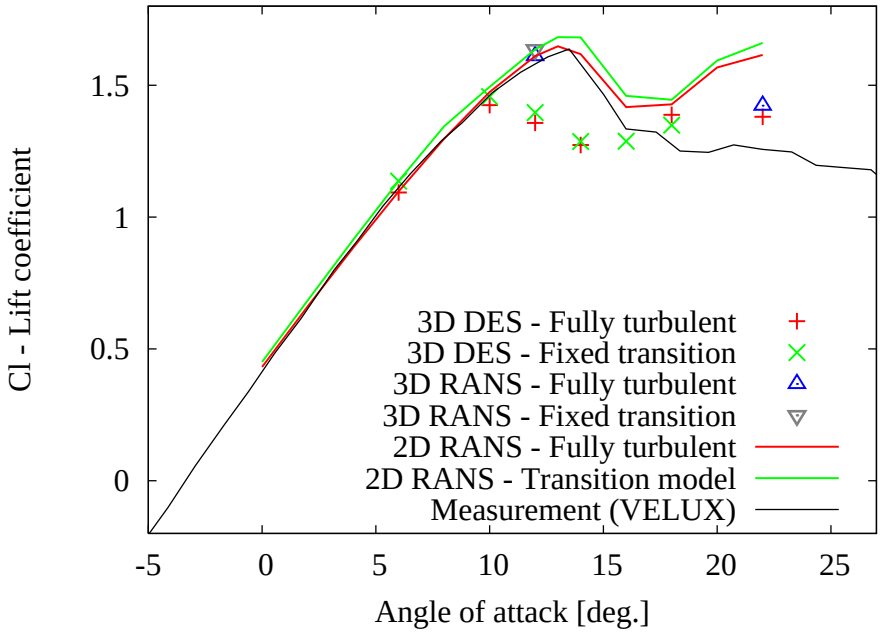

(a) Lift

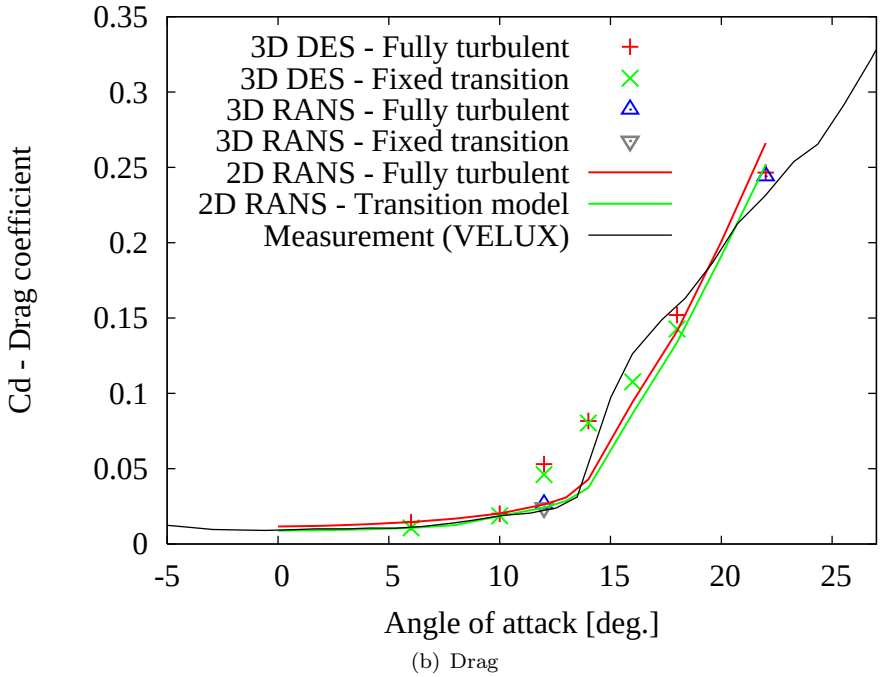

(b) Drag

Figure 6. Polar Characteristics for RISØ-B1-18 Airfoil

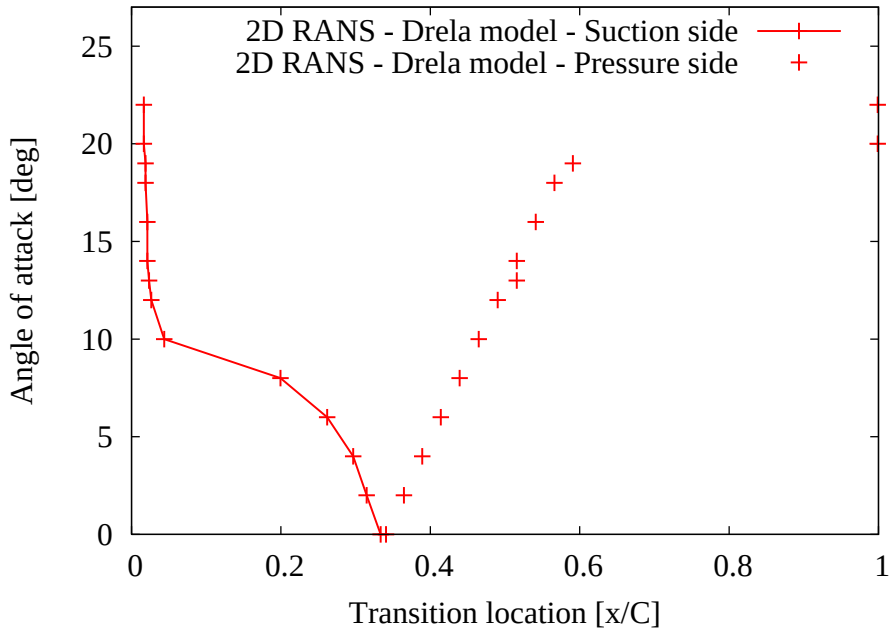

Figure 7. Transition Location for RISØ-B1-18 Airfoil

Influence of 2D/3D Computations and Turbulence modelling

Two-dimensional computational results are compared with three-dimensional ones, the latter including RANS and DES simulations. All calculations are fully turbulent. Lift and drag characteristics are displayed in Figs. 8(a-b). Pressure and skin friction coefficient distributions at several stations along the airfoil span are displayed in Figs. 9 to 12 for angles of attack equal to $\alpha = 6, 12, 18$ and 22^o, respectively.

As expected, 2D and 3D computations, and experimental results are in good agreement in the linear region before stall ($\alpha = 6$ and 10^o, Fig. 9).

At $\alpha = 12^o$, the 3D DES computation has already predicted stall occurrence when 2D and 3D RANS computations, as well as measurements, predict almost maximum lift. From the pressure and skin friction distributions (Figs. 10(a-b)), it can be seen that the flow predicted by the 3D DES model has broken up into highly three-dimensional chaotic structures, causing partial trailing edge separation at some span locations along the blade, whereas the flow field is still (or almost) attached until trailing edge at some other span locations. As a consequence, the predicted lift is smaller, and the drag higher, than in the 2D and 3D RANS cases for which the flow remains two-dimensional and attached along the whole span of the airfoil section, except for a small separated region near the trailing edge.

At $\alpha = 18^o$, relative good agreement is recovered between all computational results and the experimental ones as shown in Fig. 11. Trailing edge separation is predicted at the same location by all methods. The 3D DES computations predict only small amplitude three dimensional structures.

At $\alpha > 20^o$, the 2D RANS results predict a significant new increase of lift not observed in the 3D calculations. Fig. 12 shows that the 2D calculation exhibits a higher pressure coefficient on the suction side, in particular in the detached region. Time-series of the lift and drag displayed on Fig. 13 show that the 2D calculations does not permit the formation of long time period flow structures, which can be observed in the 3D calculations (in particular the 3D RANS). These are identified as large oscillations of the flow, which form themselves over a long period of time during which the lift is slowly building up (with a non-dimensional characteristic time approximately equal to 80 for the 3D RANS calculation). Then, a rather abrupt lift drop occurs as it can clearly be observed for the 3D RANS calculation. These larger oscillations are superimposed over the 2D vortex shedding phenomenon of much smaller time-period (with a non-dimensional characteristic time approximately equal to 1) observed for most 2D and 3D calculations, at least all 3D DES calculations, beyond stall (see for example section 3.3). It is not quite clear what physical phenomenon is responsible for this low frequency pattern. However, Figs. 14 and 15 clearly show that it is a two-dimensional phenomenon as both lift and drag time histories at several stations along the airfoil span are very well correlated, both in the case of the 3D RANS and 3D DES calculations (However, it is noteworthy that it is not captured by the 2D simulations). This particular pattern is obviously much more chaotic and three-dimensional in the latter case. In addition, the instantaneous pressure and skin friction coefficients computed at the lower and higher peak values of lift for the 3D RANS calculation are presented on Figs. 16(a-b), respectively. It can be observed that the periodic pattern originates from a slow displacement of the detachment point on the suction side, most probably corresponding to a modification of the size of the recirculation zone, and leading to a change of the pressure coefficient distribution on that side of the airfoil. The abrupt decrease of lift observed in Fig. 13(a) is then identified as the shedding of a larger vortex of the size order of the whole detached region.

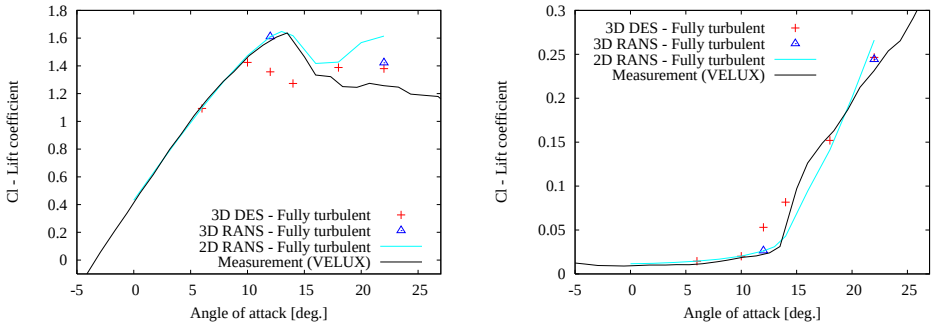

(a) Lift (b) Drag

Figure 8. Polar Characteristics - RISØ-B1-18 - Fully Turbulent Computations

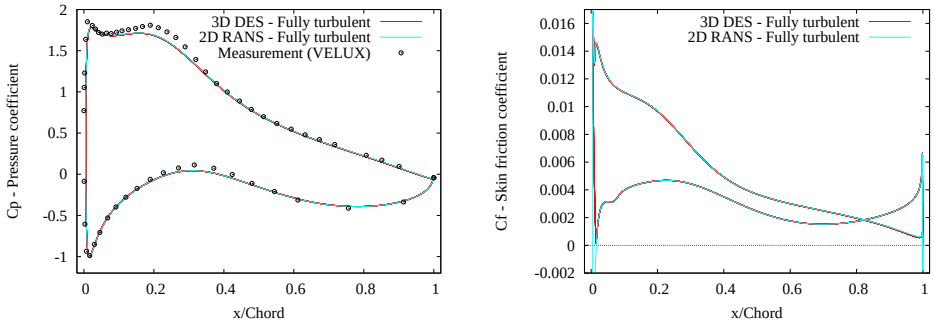

(a) Pressure Distribution - $\alpha = 06^o$ (b) Skin Friction Distribution - $\alpha = 06^o$

Figure 9. C_p and C_f Distributions - RISØ-B1-18 - Fully Turbulent - $\alpha = 06^o$

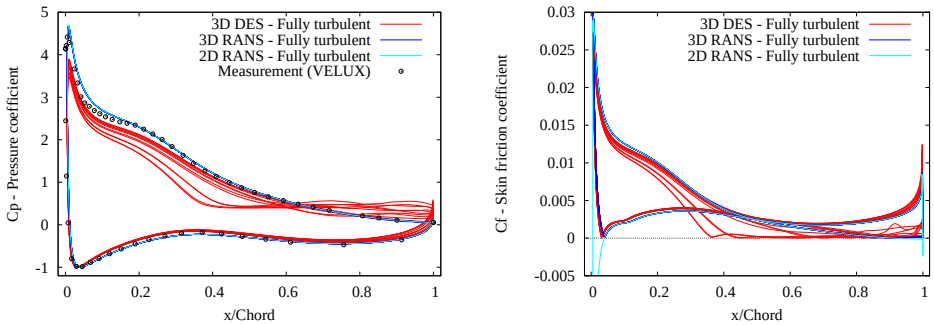

(a) Pressure Distribution - $\alpha = 12^o$ (b) Skin Friction Distribution - $\alpha = 12^o$

Figure 10. C_p and C_f Distributions - RISØ-B1-18 - Fully Turbulent - $\alpha = 12^o$

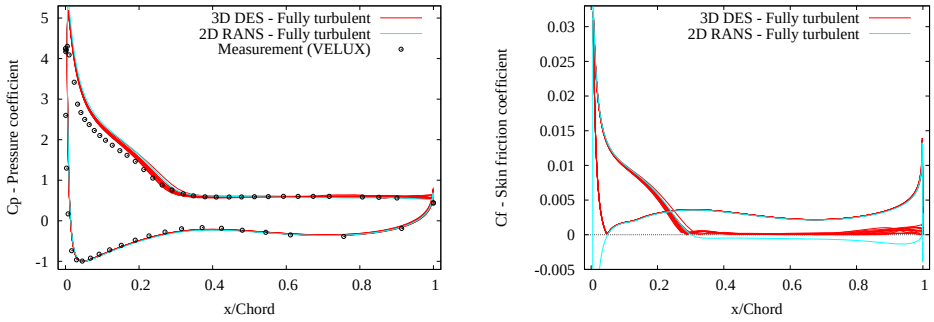

(a) Pressure Distribution - $\alpha = 18^o$ (b) Skin Friction Distribution - $\alpha = 18^o$

Figure 11. C_p and C_f Distributions - RISØ-B1-18 - Fully Turbulent - $\alpha = 18^o$

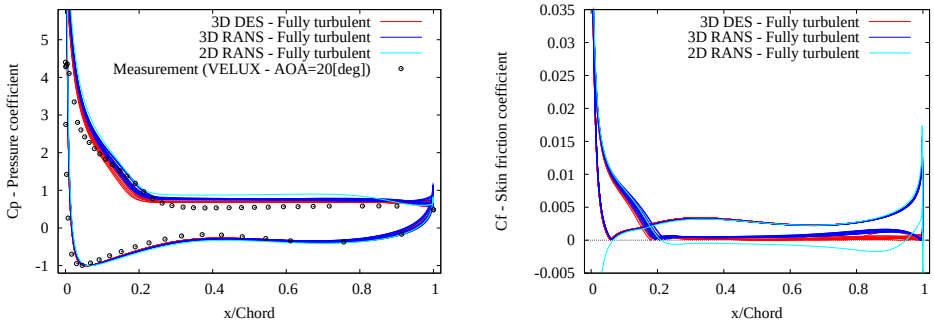

(a) Pressure Distribution - $\alpha = 22^o$ (b) Skin Friction Distribution - $\alpha = 22^o$

Figure 12. C_p and C_f Distributions - RISØ-B1-18 - Fully Turbulent - $\alpha = 22^o$

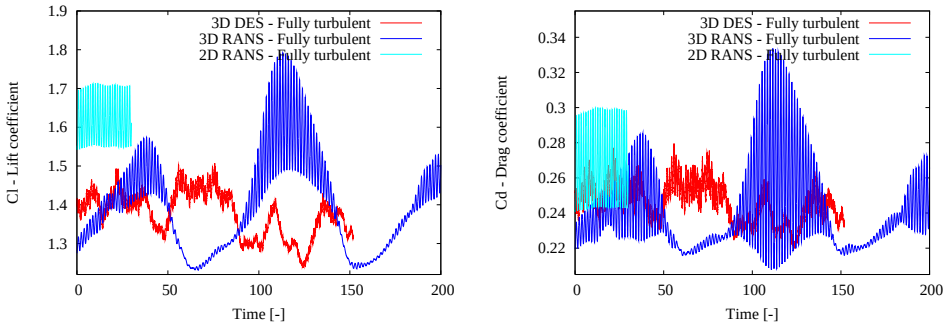

(a) Lift (b) Drag

Figure 13. Forces Time-Series along Span of RISØ-B1-18 - Fully Turbulent - $\alpha = 22^o$

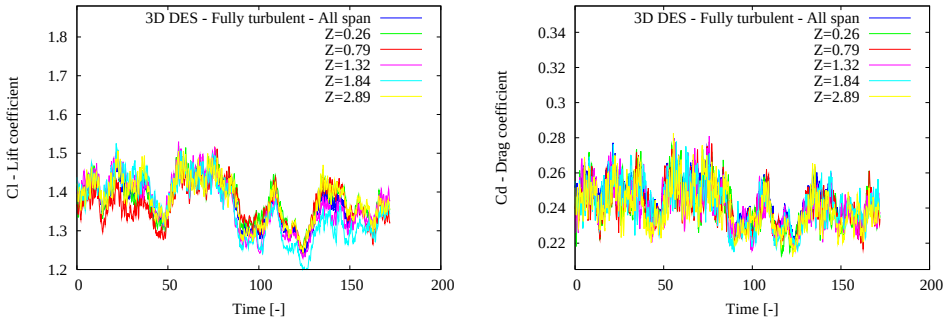

(a) Lift (b) Drag

Figure 14. Forces Time-Series along Span of RISØ-B1-18 - 3D DES - $\alpha = 22^o$

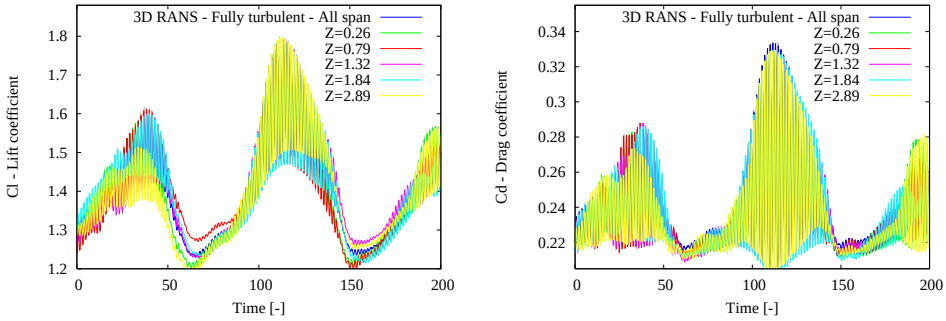

(a) Lift (b) Drag

Figure 15. Forces Time-Series along Span of RISØ-B1-18 - 3D RANS - $\alpha = 22^o$

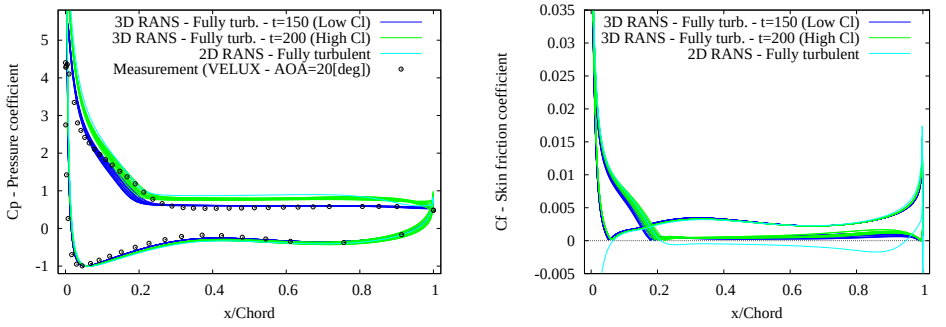

(a) Pressure Distribution - $\alpha = 22^o$ (b) Skin Friction Distribution - $\alpha = 22^o$

Figure 16. C_p and C_f Distributions - RISØ-B1-18 - 3D RANS - Low and high C_l - $\alpha = 22^o$

Influence of Transition Model

The influence of the transition model is studied, first for 3D computations, then for 2D computations.

Lift and drag characteristics for the 3D computations are reported on Fig. 17. Pressure and skin friction coefficient distributions at angles of attack equal to $\alpha = 6, 12$ and 18^o are displayed in Figs. 18 to 20, respectively.

At $\alpha = 6^o$, it can be seen on Fig. 18(b) that transition is enforced on the suction side at approximately 1/4 of the chord length. However, this has a small impact on the pressure distribution (Fig. 18(a)) and consequently the predicted lift. Remind that insensitivity to transition location was one of the design objectives of this airfoil profile.

At $\alpha = 12^o$, the scenario concerning stall occurrence described in section 4.2 can be observed again. 3D RANS computations exhibit results close to the experimenal ones (both in the fully turbulent case and with transition model), and the 3D DES computation with transition model appears to be more three-dimensional and chaotic than the fully turbulent one (see Fig. 19).

Results presenting 2D calculations are plotted in Fig. 21 for the lift and drag, and in Figs. 22 to 24 for the pressure and skin friction coefficient distributions. Similar conclusions as in the 3D RANS computational cases can be drawn.

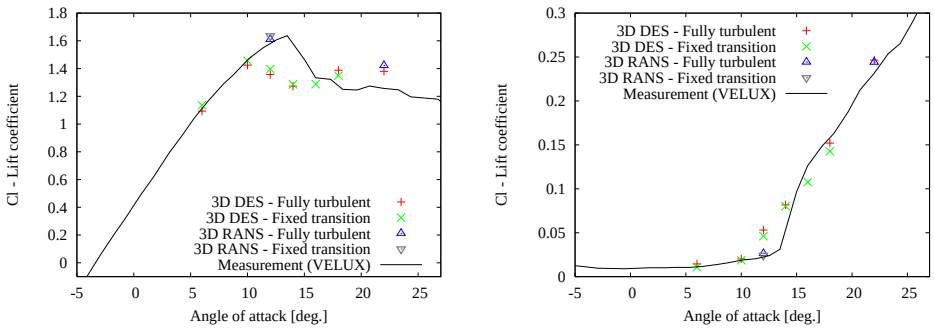

(a) Lift (b) Drag

Figure 17. Polar Characteristics - RISØ-B1-18 Airfoil - 3D Computations

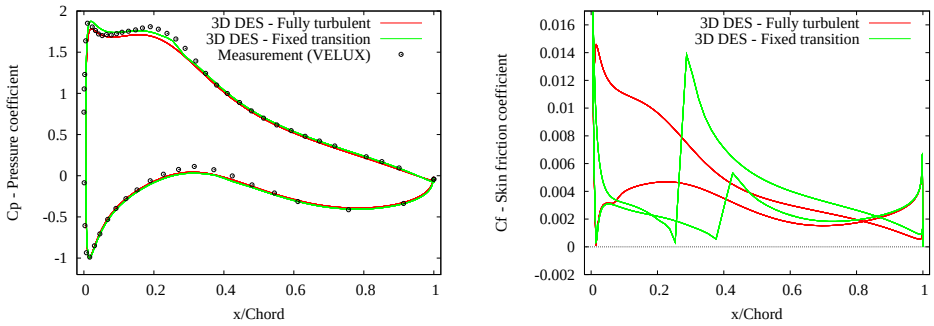

(a) Pressure Distribution - $\alpha = 06^o$ (b) Skin Friction Distribution - $\alpha = 06^o$

Figure 18. C_p and C_f Distributions - RISØ-B1-18 - 3D Computations - $\alpha = 06^o$

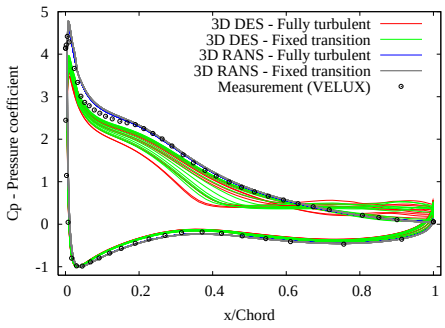

(a) Pressure Distribution - $\alpha = 12^o$

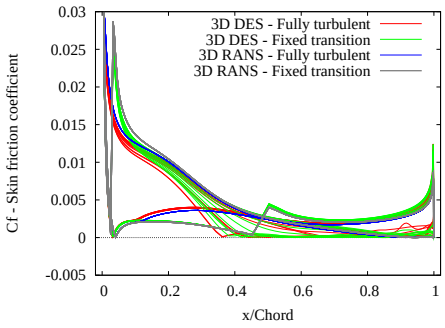

(b) Skin Friction Distribution - $\alpha = 12^o$

Figure 19. C_p and C_f Distributions - RISØ-B1-18 - 3D Computations - $\alpha = 12^o$

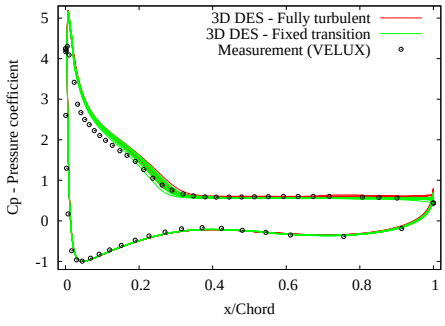

(a) Pressure Distribution - $\alpha = 18^o$

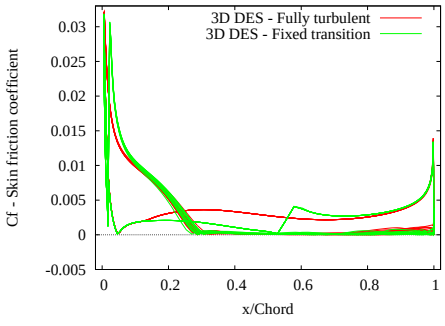

(b) Skin Friction Distribution - $\alpha = 18^o$

Figure 20. C_p and C_f Distributions - RISØ-B1-18 - 3D Computations - $\alpha = 18^o$

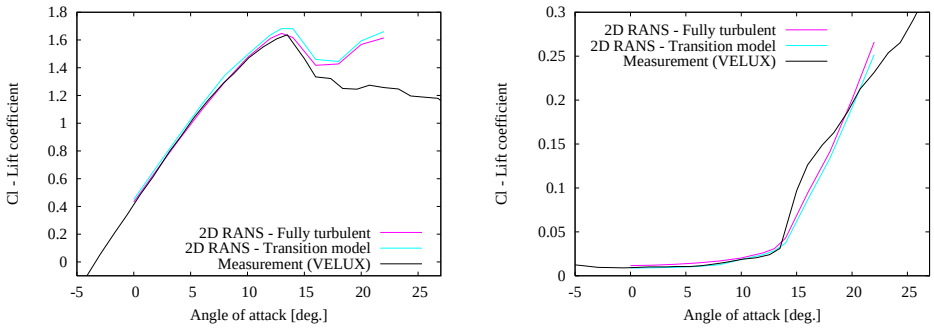

(a) Lift (b) Drag

Figure 21. Polar Characteristics - RISØ-B1-18 Airfoil - 2D Computations

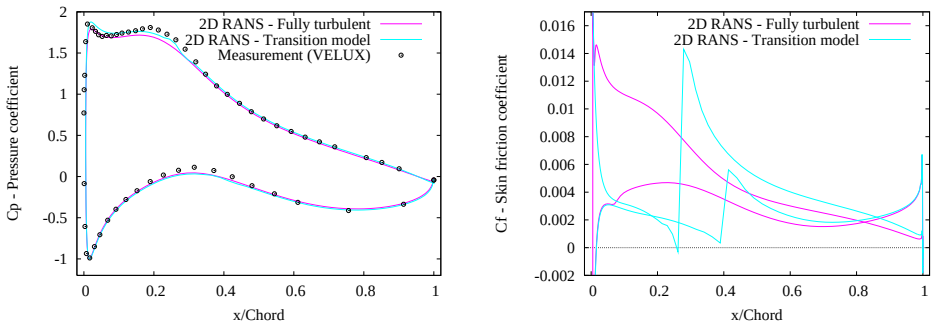

(a) Pressure Distribution - $\alpha = 06^o$ (b) Skin Friction Distribution - $\alpha = 06^o$

Figure 22. C_p and C_f Distributions - RISØ-B1-18 - 2D Computations - $\alpha = 06^o$

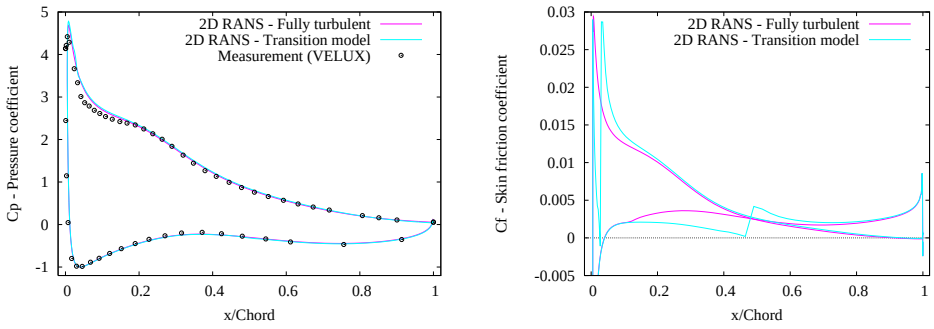

(a) Pressure Distribution - $\alpha = 12^o$ (b) Skin Friction Distribution - $\alpha = 12^o$

Figure 23. C_p and C_f Distributions - RISØ-B1-18 - 2D Computations - $\alpha = 12^o$

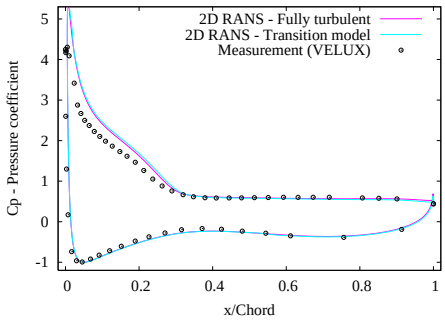

(a) Pressure Distribution - $\alpha = 18^o$

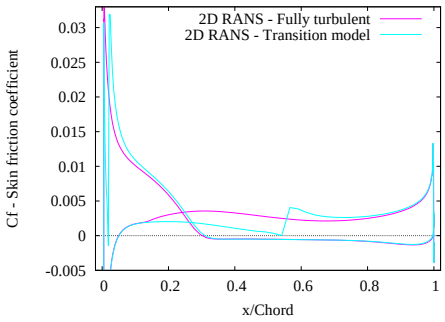

(b) Skin Friction Distribution - $\alpha = 18^o$

Figure 24. C_p and C_f Distributions - RISØ-B1-18 - 2D Computations - $\alpha = 18^o$

4.3 Summary of Results

This airfoil is characterized by its insensitivity to transition location, which was one of the objectives for its design. This characteristic is well reflected by the numerical calculations. Moreover, there is a general fairly good agreement between the experimental and the computational results. However, two major discrepancies are observed. Firstly, the 3D DES computations (with or without transition modelling) predict stall occurrence too early. Secondly, the 2D RANS calculations predict a continued increase of lift for high angles of attack ($\alpha > 20^o$) which is certainly non-physical, whereas 3D DES calculations are able to reproduce the correct chaotic three-dimensional structures of the fully detached flow.

5 Results for the NACA 63-430 Airfoil

This 30% thick airfoil belongs to the NACA wing section family. It has been measured in the VELUX wind tunnel [5], which is an open test section wind tunnel, and has a background turbulence level of 1%. The testing facility is described in Fuglsang *et al* [6]. The Reynolds number of the experiment, and of the computations, is equal to 1.5×10^6. The airfoil section test stand was such that the span width of the airfoil was 3.2 chord lenths, and end plates were fixed at the ends of the airfoil to limit 3D flow effects.

This particular airfoil was chosen as large discrepancies between experimental results and 2D numerical computations were observed in the Wind Turbine Airfoil Catalogue [1].

5.1 Test cases

The 3D computations were performed with both the $k-\omega$ SST turbulence model (RANS computations) and the DES turbulence model. In addition to fully turbulent computations, the influence of the implementation of a transition model is investigated. The fixed transition and the simplified transition models are both studied, with transition locations extracted from 2D calculations with the transition model by Drela [4] implemented as described in [13]. In all computations, the time-step is set to $\Delta t = 0.01$.

5.2 Results

Lift and drag characteristics for all computations are gathered in Figs. 25(a-b). It is quite clear that there exist large discrepancies between the different computational results.

Transition locations predicted in the 2D RANS calculations with the model by Drela are plotted on Fig. 26(a), together with the predictions from the simplified transition model in the 3D DES computations. The discrepancies between the two models is getting larger from $\alpha = 10^o$, i.e. when stall starts to occur. Although the transition locations predicted by the simplified transition model are extracted from the 2D RANS calculations with Drela's model (see description of the simplified transition model in section 2.2), these discrepancies are caused by the downwash created by the three-dimensional airfoil wake which modifies the flow around the airfoil, including the stagnation point location on the pressure side near the leading edge of the airfoil as illustrated in Fig. 26(b). This stagnation location is actually used for interpolating the transition location within the simplified model, which thus differs from the two-dimensional case and the fixed transition model. The modification of the transition location modifies in turn the flow around the airfoil and the airfoil wake. In the end, the final transition location predicted by the simplified model represents an equilibrium between the computed stagnation point location, airfoil wake and transition location.

In the following of this section, the time-series of the aerodynamic forces, the influence of the turbulence model, and finally of the transition model, are investigated.

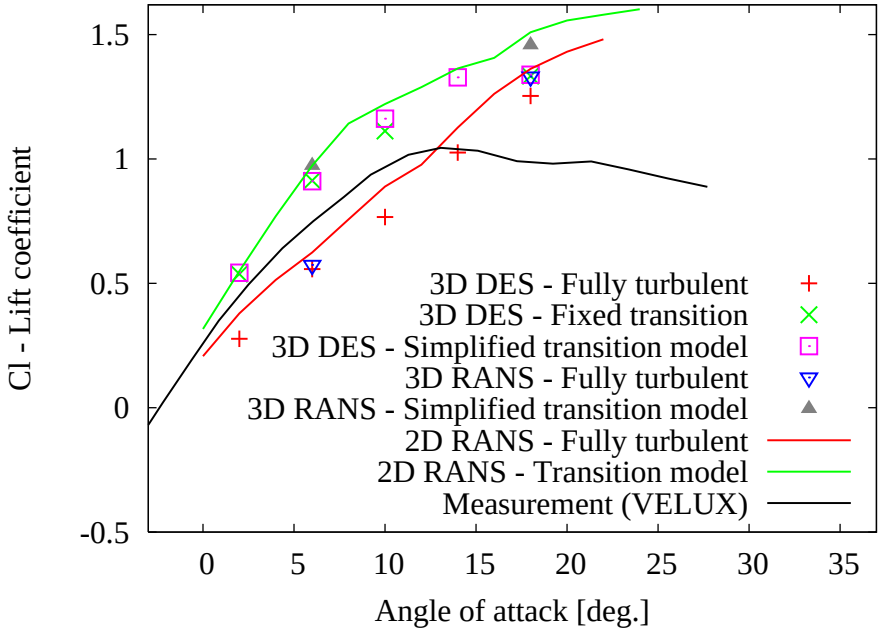

(a) Lift

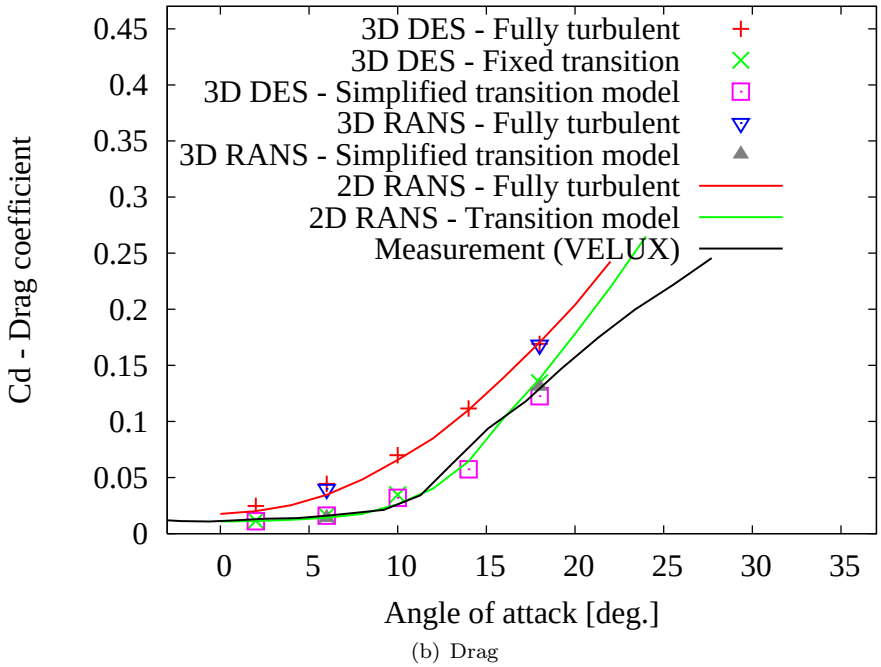

(b) Drag

Figure 25. Polar Characteristics for NACA 63-430 Airfoil

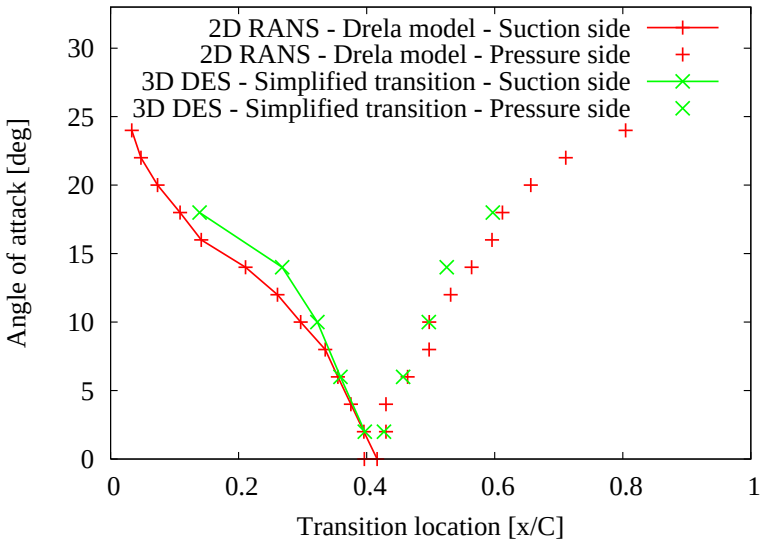

(a) Transition Location

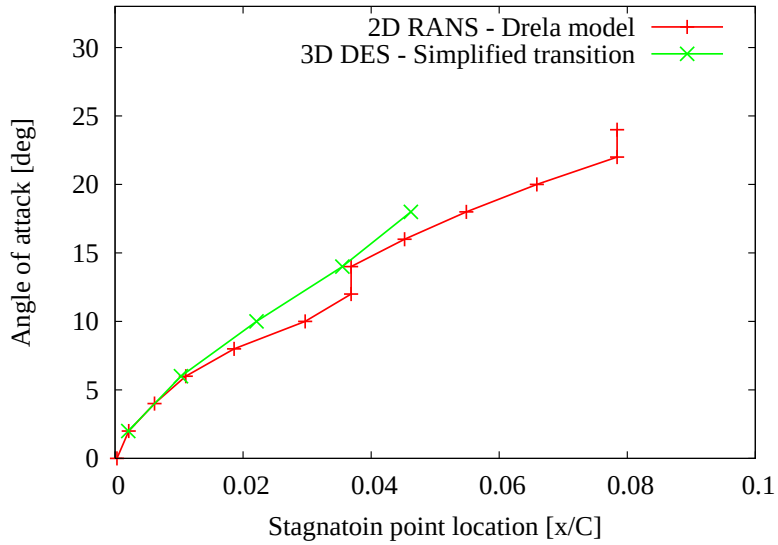

(b) Stagnation Point Location

Figure 26. Transition and Stagnation Point Locations for NACA 63-430 Airfoil

Time-Series of Aerodynamic Forces

The lift and drag (averaged over the airfoil span) time-series for the 3D fully turbulent computations and with the simplified transition model, both with RANS and DES models, are plotted in Figs. 27 and 28 for angles of attack equal to 6 and 18^o, respectively. The data for the 2D RANS computations with transition model are added. It can be seen that, at $\alpha = 6^o$, all RANS (2D and 3D) computations predict an almost steady flow, whereas the DES computations predict some degree of unsteadiness, in particular the fully turbulent one. The latter exhibits a longer transient, which can be seen at the beginning of the plotted time-series. At $\alpha = 18^o$, both RANS and DES computations exhibit unsteadiness. However, RANS computations predict quasi-periodic flow patterns, whereas the DES computations predict more chaotic flow patterns. It can be noted that, even if the 2D and 3D RANS computations with transition model give similar results in average, the amplitude of the oscillations are twice as large for the 2D calculations for $\alpha = 18^o$ (see below for a discussion on these oscillations).

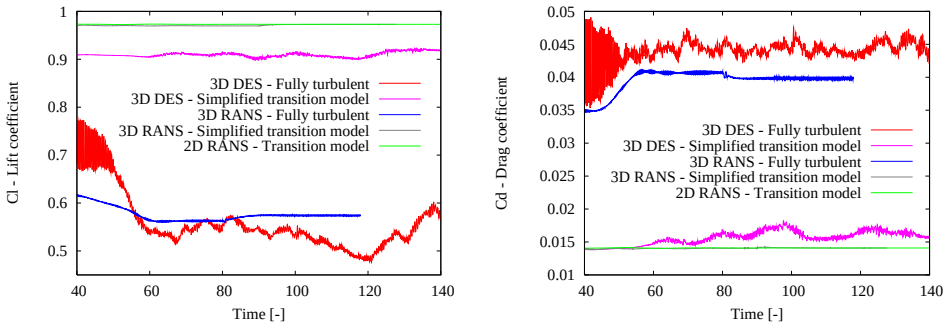

(a) Lift (b) Drag

Figure 27. Lift and Drag Time-Series - NACA 63-430 Airfoil - $\alpha = 06^o$

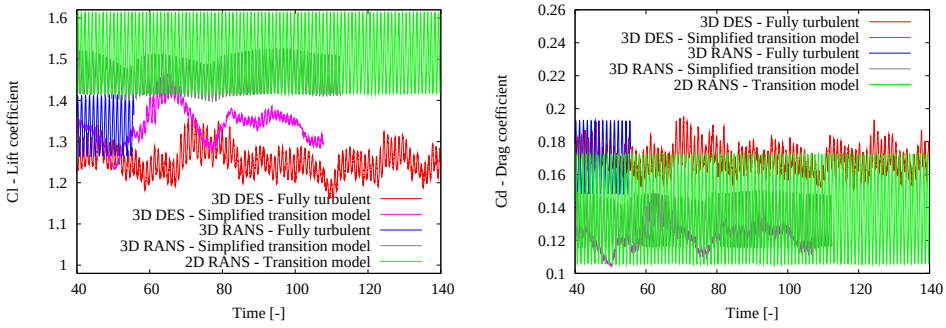

(a) Lift (b) Drag

Figure 28. Lift and Drag Time-Series - NACA 63-430 Airfoil - $\alpha = 18^o$

Details of the time-series for the different 3D configurations are now displayed for the lift averaged on the airfoil span, and at several locations along the span of the airfoil, on Figs. 29 and 30 for angles of attack equal to 6 and 18^o, respectively. It can be noted that the fully turbulent 3D RANS computation at $\alpha = 6^o$ (Fig. 29(c)) exhibits a 3D pattern as the lift, even if constant in time, is not constant along the span of the airfoil. For all computed flow configurations that exhibit unsteady effects (all cases at $\alpha = 18^o$ and 3D DES at $\alpha = 6^o$), the presence of a two-

dimensional flow pattern is also noteworthy. This phenomenon can be observed as oscillations of period approximately equal to $T = 1$ (slightly lower for $\alpha = 6^o$), which are in phase between all stations along the span of the airfoil. This was identified as a two-dimensional vortex shedding phenomenon in a previous work [2, 3]. The amplitude of these lift oscillations are quite similar for all computations at $\alpha = 18^o$ indicating that it is the same phenomenon happening in all cases, although it can be seen that their amplitudes can momentarily decrease for the 3D DES computations with simplified transition model (Fig. 30(b)). Note that this vortex shedding is the only cause of unsteadiness for the fully turbulent RANS computations at $\alpha = 18^o$ as the lift oscillations are identical along the span of the airfoil and fully periodic.

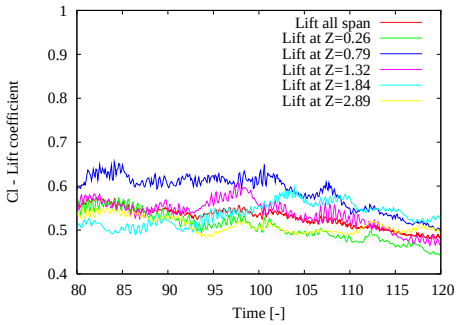

(a) 3D DES Computation - Fully Turbulent

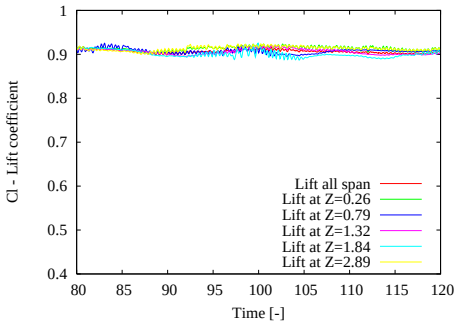

(b) 3D DES Computation - Simplified Transition

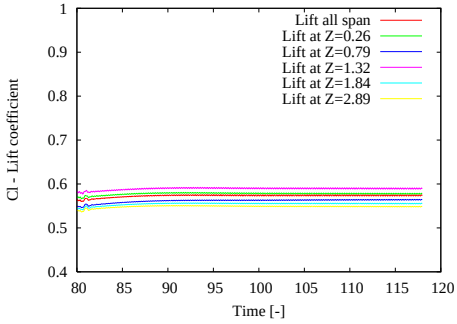

(c) 3D RANS Computation - Fully Turbulent

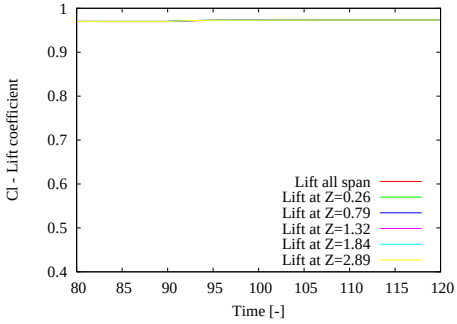

(d) 3D RANS Computation - Simplified Transition

Figure 29. Lift Time-Series along Span - NACA 63-430 Airfoil - α=06^o

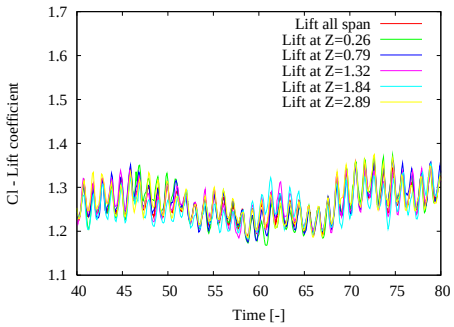

(a) DES Computation - Fully Turbulent

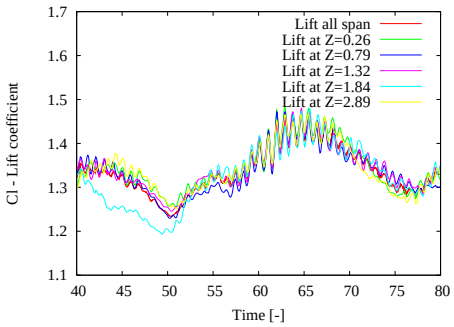

(b) DES Computation - Simplified Transition

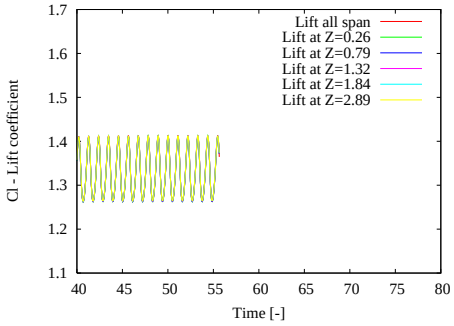

(c) RANS Computation - Fully Turbulent

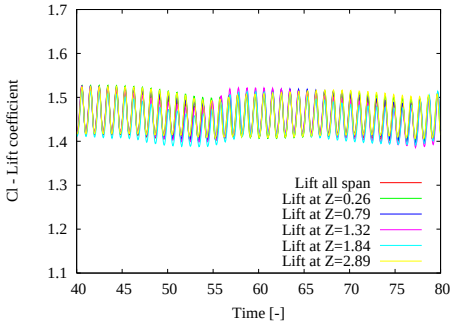

(d) RANS Computation - Simplified Transition

Figure 30. Lift Time-Series along Span - NACA 63-430 Airfoil - $\alpha = 18^o$

Effect of the Turbulence Model

In this section, the influence of the turbulence model (RANS or DES models) is investigated. 2D computations are also displayed.

Firstly, only fully turbulent computations are considered. Fig. 31 shows the polar characteristics, whereas Figs. 32 and 33 display the pressure and skin friction coefficient distributions (at several locations along the span of the airfoil for 3D computations) at $\alpha = 6$ and 18^o, respectively.

It can be seen that there is a good agreement between all computational methods (2D and 3D RANS, and 3D DES). Nevertheless, if computational results and measurements exhibit somehow a similar lift slope in a short range of angles of attack ($\alpha = 4$ to 10^o), there exists a rather large level offset, the computational results predicting a lower lift than the measurements. Moreover, after stall, all computational results predict a continued increase of lift.

Pressure and skin friction distributions reveal that computational methods predict a large trailing edge separation occurring already at $\alpha = 6^o$ (Fig. 32). However the measured experimental pressure coefficient distribution indicates that such a trailing edge separation does not occur before stall. But this does occur after stall ($\alpha = 18^o$, Fig. 33) both in the experiment and in the computations. After stall, the higher lift predicted by numerical methods is obviously caused by a too high pressure coefficient on the suction side of the airfoil, in particular in the region between the leading edge of the airfoil and the trailing edge separation point. These discrepancies between numerical results and measurements might originate from the presence of a laminar separation near the leading edge on the suction side in the experiment. As a consequence, the boundary layer might get considerably thicker resulting in a higher pressure coefficient loss downstream. Another possible explaination for these discrepancies might be the occurrence of a by-pass transition phenomenon in the wind tunnel caused by the turbulence intensity of 1% as it was measured in the test stand [6]. Remind that there is no free-stream turbulence in the numerical computations.

It can also be observed that three-dimensional chaotic flow patterns do occur near the trailing edge of the airfoil for the 3D DES computations, and are not present in the 3D RANS computations for $\alpha = 18^o$.

Secondly, the influence of the turbulence model is investigated when a transition model is implemented. Polar characteristics are plotted in Fig. 34, when Figs. 35 and 36 display the pressure and skin friction coefficient distributions (at several locations along the span of the airfoil for 3D computations) at $\alpha = 6$ and 18^o, respectively.

In this case, all computational results predict a too high lift at all angles of attack. At $\alpha = 6^o$, the higher pressure coefficient predicted by the computational methods might originate from a transition location predicted too far downstream in the boundary layer as indicated by Fig. 35. Indeed, it was shown that a by-pass transition model (for 2D RANS calculations) was performing much better when applied to the simulation of this particular airfoil [13]. At higher angle of attack ($\alpha = 18^o$), the same scenario described above with laminar separation present in the experiment but not in the fully turbulent computations might occur again, as well as a too far downstream transition location predicted by the transition model.

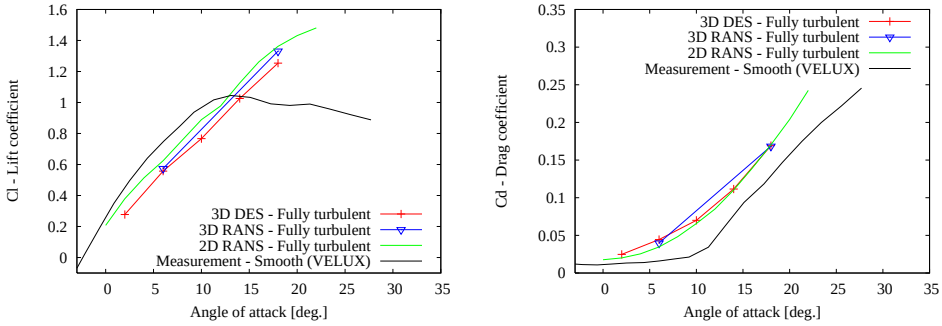

(a) Lift (b) Drag

Figure 31. Polar Characteristics - NACA 63-430 - Fully Turbulent Computations

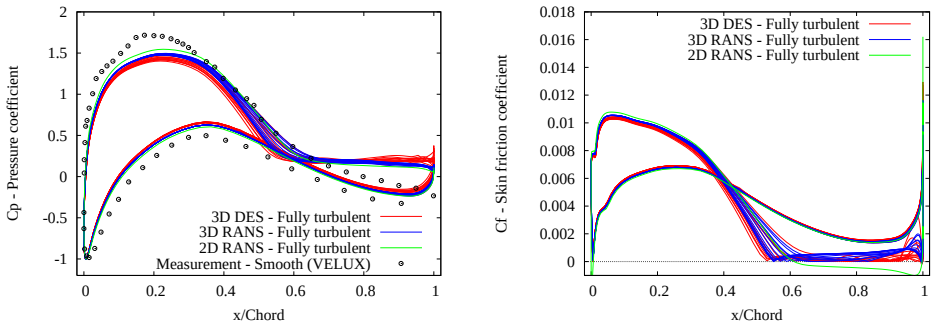

(a) Pressure Distribution - $\alpha = 06^o$ (b) Skin Friction Distribution - $\alpha = 06^o$

Figure 32. C_p and C_f Distributions - NACA 63-430 - Fully Turbulent - $\alpha = 06^o$

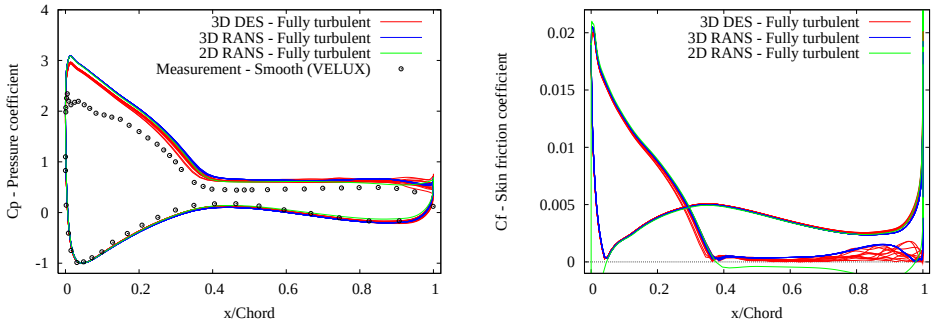

(a) Pressure Distribution - $\alpha = 18^o$ (b) Skin Friction Distribution - $\alpha = 18^o$

Figure 33. C_p and C_f Distributions - NACA 63-430 - Fully Turbulent - $\alpha = 18^o$

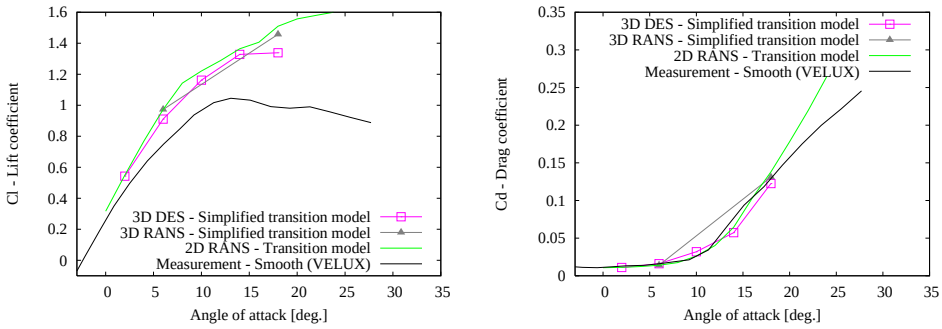

(a) Lift (b) Drag

Figure 34. Polar Characteristics - NACA 63-430 Airfoil - With Transition Model

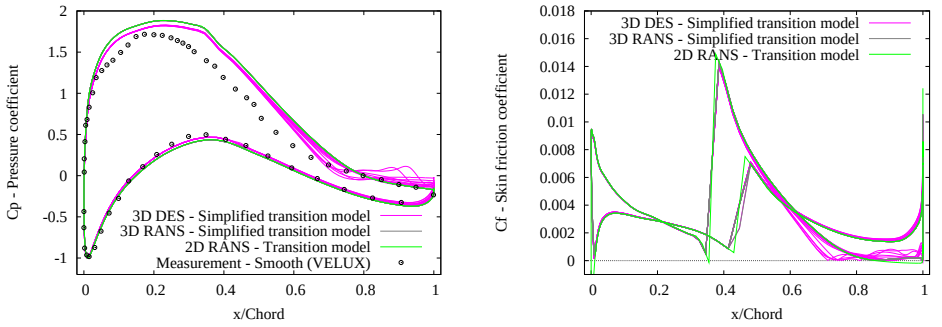

(a) Pressure Distribution - $\alpha = 06^o$ (b) Skin Friction Distribution - $\alpha = 06^o$

Figure 35. C_p and C_f Distributions - NACA 63-430 - Transition Model - $\alpha = 06^o$

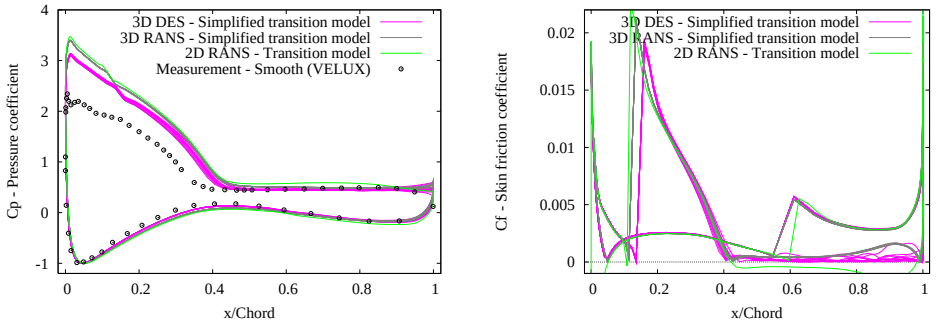

(a) Pressure Distribution - $\alpha = 18^o$ (b) Skin Friction Distribution - $\alpha = 18^o$

Figure 36. C_p and C_f Distributions - NACA 63-430 - Transition Model - $\alpha = 18^o$

Effect of the Transition Model

In this section, the influence of the transition modelling is investigated for the 3D DES computations. Fig. 37 presents the polar characteristics, whereas Figs. 38 and 39 display the pressure and skin friction coefficient distributions at several locations along the span of the airfoil at $\alpha = 6$ and 18^o, respectively.

It can be seen that the discrepancies between the computations with and without transition model for the pressure coefficient distribution are great even at lower angle of attack ($\alpha = 6^o$, Fig. 38(a)), resulting in a higher lift prediction for the computations with transition model. This is due to the transition to turbulence located quite far downstream (at $x/C \approx 0.35$) and preventing the development of a thicker turbulent boundary layer upstream this transition location as in the fully turbulent case, which in turn increases the pressure coefficient on the suction side, and therefore increases the lift. This modification of pressure on the airfoil suction side is directly related to the thickness of the boundary layer which modifies the curvature of the streamlines in the flow field in the vicinity of the boundary layer. Thereby, the pressure distribution in the flow field is also modified, with a direct impact on the airfoil surface pressure distribution. As it can be seen on Figs. 38(a-b), the computations with fixed transition predict a smaller trailing edge separation in comparison to the fully turbulent results, but which seems to be in better agreement with the experimental results as indicates the pressure coefficient distribution in the vicinity of the trailing edge on the suction side. However, the transition location might be enforced too far downstream as there is a poor agreement of the pressure coefficients before separation occurs. On the pressure side, which is usually much less sensitive to the transition location, there is anyhow a quite large discrepancy between the fully turbulent computation and the one with fixed transition. Nevertheless, the measured pressure coefficient and computational results with fixed transition are very close to each other, indicating the need for a transition model on the pressure side in this case.

At higher angle of attack ($\alpha = 18^o$, Fig. 39), the discrepancies are less noticeable between fully turbulent computation and computation with transition. The pressure coefficient distributions around the airfoil contour are distributed in a slightly different way for the computations with and without transition. Moreover, the measured pressure coefficient is quite lower than the computed ones before separation occurs, most probably due to the higher turbulence level in the wind tunnel combined with the difficulty to accurately predict the transition location (possible occurrence of a by-pass transition as noticed in the previous section), or possibly due to the presence of a leading edge laminar separation bubble in the experiment.

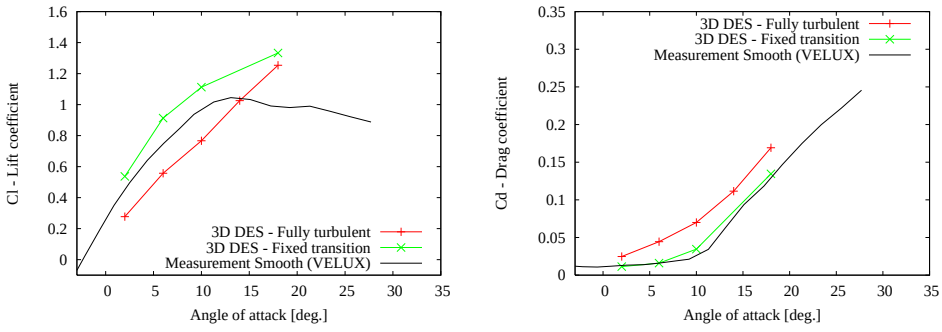

(a) Lift (b) Drag

Figure 37. Polar Characteristics - NACA 63-430 Airfoil - Influence of Transition

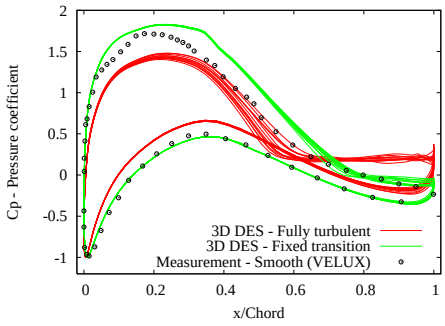

(a) Pressure Distribution - $\alpha = 06^o$

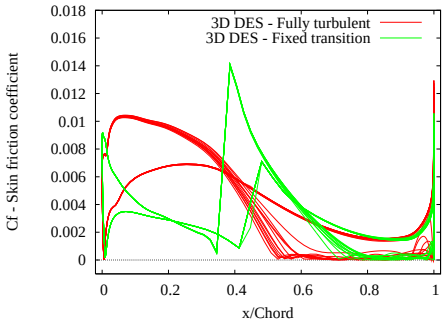

(b) Skin Friction Distribution - $\alpha = 06^o$

Figure 38. C_p and C_f Distributions - NACA 63-430 Airfoil - $\alpha = 06^o$

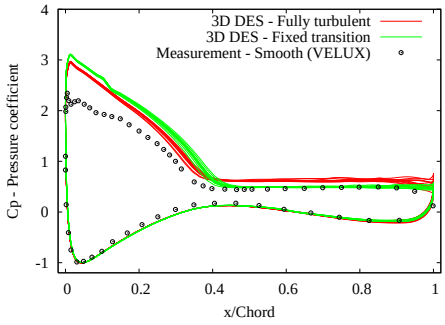

(a) Pressure Distribution - $\alpha = 18^o$

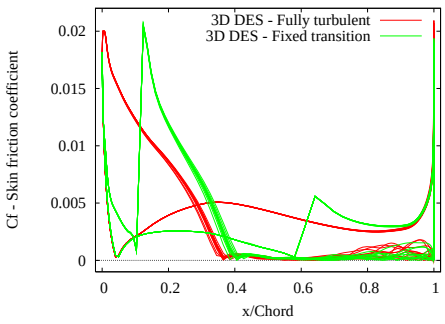

(b) Skin Friction Distribution - $\alpha = 18^o$

Figure 39. C_p and C_f Distributions - NACA 63-430 Airfoil - $\alpha = 18^o$

Leading Edge Roughness

A central problem in the calculations seems to be the inaccurate prediction of transition location. In most cases in this report, it is extracted from 2D computations, but yet it is not given that these data are accurate and in accordance with the experimental results (except for S809 airfoil for which transition location was measured during the experiment before stall, see section 6).

In order to emulate leading edge roughness, the airfoil section was equipped with a so-called trip-tape during the VELUX wind tunnel measurements [5]. It can as well be viewed as a device which is able to trigger transition of the boundary layer at a fixed location. However, the amount of turbulence introduced in the boundary layer is not well defined, and this could actually correspond to a perturbation intensity corresponding to a natural transition occurring upstream in the boundary layer along the airfoil surface. Nevertheless, the experimental results are herein compared with computational results obtained with a fixed transition for which the transition location is the same as the position of the trip-tape. In our case, it is located at 0.05 chord length on the suction side, and 0.3 chord on the pressure side. These numerical results will be referred as *trip-tape transition*.

Lift and drag characteristics are displayed in Figs. 40(a-b) for 3D DES computations together with experimental data. It can be seen that the computational results with trip-tape transition are nearly identical to fully turbulent calculations, indicating the fact that the transition location is relatively too close to the leading edge to make any difference with a fully turbulent boundary layer. The computed lift and drag are quite close to the measurements with trip-tape until an angle of attack of 6^o. However, beyond that point, the computed lift keeps the same ascending slope, whereas the slope of the measured lift starts to slowly decay.

The pressure and skin friction coefficient distributions for $\alpha = 6, 14$ and 18^o are plotted on Figs. 41 to 43, respectively. As expected, at low angle of attack ($\alpha = 6^o$, Fig. 41), the pressure coefficient measured for the airfoil equipped with trip-tape is lower on the suction side, than for the smooth airfoil. Moreover, it can be seen that in this case, there exists a trailing edge separation which starts approximately at the same place as for the computational results for the fully turbulent configuration and with trip-tape transition. According to the pressure distribution (Fig. 41(a)), the experimental results with trip-tape exhibit as well a recirculation zone starting approximately at the same point. However, the pressure upstream this point is slightly lower. At angles of attack $\alpha = 14$ and 18^o, fully turbulent computations and computations with trip-tape transition give again very similar results. However, in this case the experimental data depart noticeably from these results. Indeed, even though the trailing edge separation is approximately well predicted, the computed pressure coefficient levels on the suction side upstream the separation point are quite higher than the experimental ones (both with and without trip-tape). It is quite clear from these and previous results that the turbulence level introduced by the trip-tape device must be quite high compared to what can be simulated in the computations, as well as to the measurements with smooth airfoil. Moreover, it must be noted that there are no external turbulent disturbances in the computations which probably amplify the observed discrepancies.

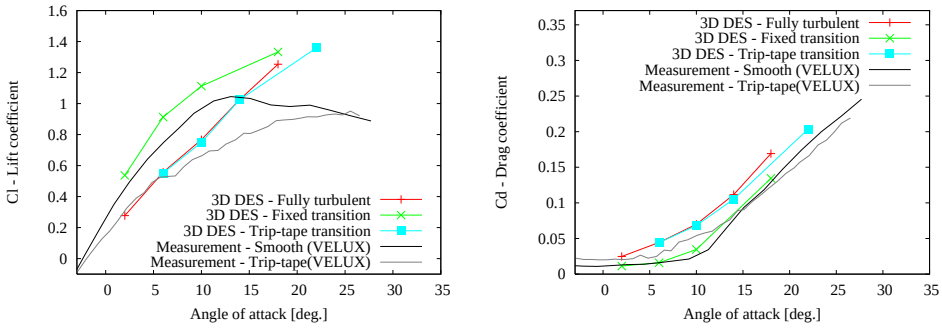

(a) Lift (b) Drag

Figure 40. Polar Characteristics - NACA 63-430 - Leading Edge Roughness

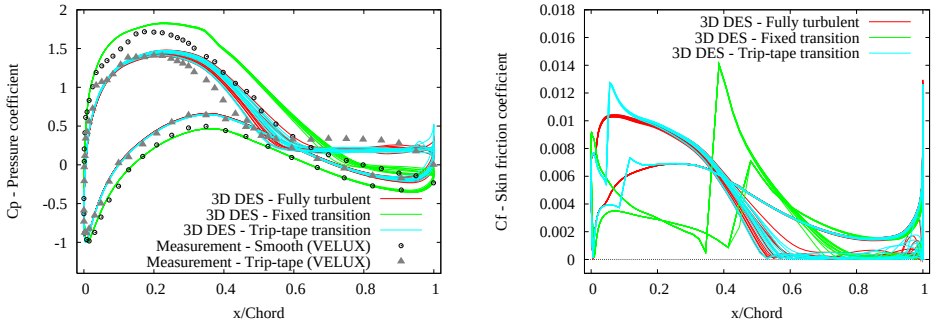

(a) Pressure Distribution - $\alpha = 06^o$ (b) Skin Friction Distribution - $\alpha = 06^o$

Figure 41. C_p and C_f Distributions - NACA 63-430 - L.E. Roughness - $\alpha = 06^o$

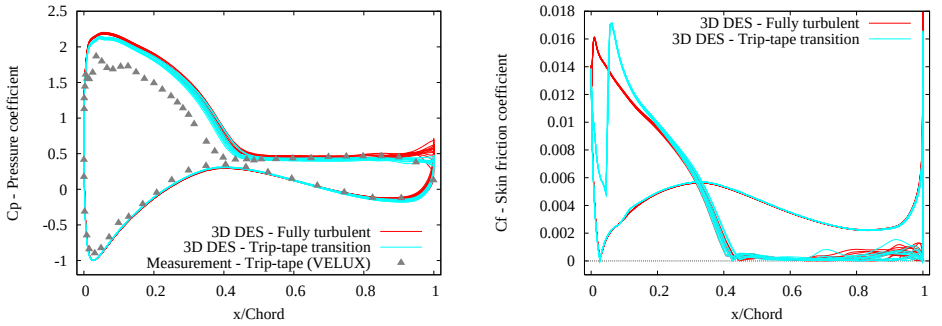

(a) Pressure Distribution - $\alpha = 14^o$ (b) Skin Friction Distribution - $\alpha = 14^o$

Figure 42. C_p and C_f Distributions - NACA 63-430 - L.E. Roughness - $\alpha = 14^o$

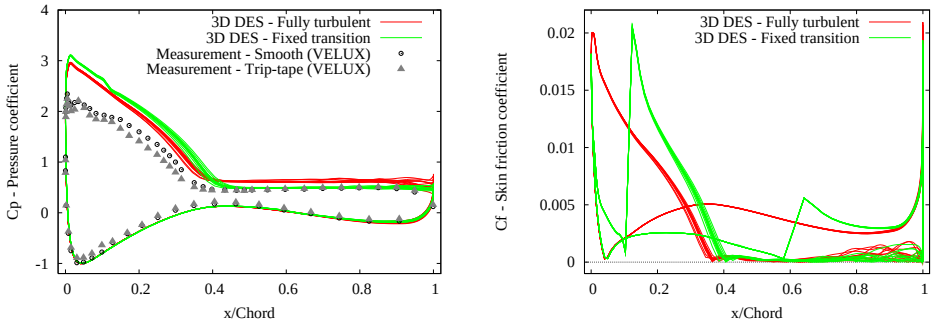

(a) Pressure Distribution - $\alpha = 18^o$ (b) Skin Friction Distribution - $\alpha = 18^o$

Figure 43. C_p and C_f Distributions - NACA 63-430 - L.E. Roughness - $\alpha = 18^o$

5.3 Summary of Results

The analysis of the results is quite difficult for this particular airfoil, and there is a poor agreement between the experimental and computational results.

RANS and DES computations give quite similar results in average. Nevertheless, the 3D DES computations allow the formation of chaotic three-dimensional structures which are not present in 3D RANS computations. There is no significant improvement by using 3D RANS simulations compared to 2D RANS in average, but 2D computations exhibit non-physical large amplitude oscillations at high angles of attack.

This airfoil is highly dependent to transition location as shown by the numerical results. The poor agreement with experimental data probably originates from a bypass transition phenomenon which is not modelled in the computations, combined with the free-stream turbulence present in the wind tunnel and not modelled in the computations.

6 Results for the S809 Airfoil

The S809 airfoil is a 21% thick wind turbine airfoil that has been designed at the National Renewable Energy Laboratory (NREL), Colorado, USA, by Somers [20]. The airfoil was tested in the low-turbulence wind tunnel at Delft University of Technology in The Netherlands [20]. The Reynolds number of the experiments that is considered in this study is $Re = 1.0 \times 10^6$, and the experimental results were obtained with free transition. Note that it is the only airfoil studied for which experimental measurement data include the transition location, which will be used in the fixed transition model when performing numerical simulations in this section. Note also that the transition location was measured to angles of attack up to 10^o before stall occurs. The span width of the wind-tunnel model section was approximately 2 chord lengths.

6.1 Test cases

The computations were first performed with the DES turbulence model. All angles of attack are computed in a fully turbulent configuration. The fixed transition model with transition locations extracted from measurements [20] is used for angles of attack $\alpha = 4$ to 10^o. Above that angle, the transition locations predicted by 2D RANS calculations with the transition model by Drela [4], implemented as described in [13], were used.

In addition, calculations are performed with the $k - \omega$ SST turbulence model (3D RANS calculation) for angles of attack equal to 10 and 18^o. Both the fully turbulent configuration and the fixed transition model are used.

Two-dimensional RANS computations are also performed for the whole range of angle of attack both in a fully turbulent configuration and with transition model.

Time-step is always set equal to $\Delta t = 2 \times 10^{-2}$.

6.2 Results

Lift and drag characteristics for all computations are gathered in Figs. 44(a-b).

Before stall occurs, slight discrepancies between the slope of lift predicted by fully turbulent computations and those with transition model can be observed. This is valid both for 2D RANS and 3D DES computations. However, 2D RANS and 3D DES computations are consistent with each other, both with and without the use of a transition model. The measurements are in good agreement with computational results obtained with transition model.

Stall initiates around $\alpha = 6$ to 8^o in the experiment. Beyond that angle of attack, the experimental lift slowly levels until $\alpha = 10^o$ before a small stall lift drop. Then it starts to slightly increase again, and finally drops again to the level measured just after the initial stall. As the angle of attack increases beyond stall, the 2D RANS computations exhibit a continued growth of lift with a slightly smaller slope than before stall. The 3D fully turbulent DES exhibits a similar behavior. However, as stall occurs at $\alpha = 10^o$, the computed lift slope is decreased (which does not occur for the 2D case), resulting in a computed lift very close to the experimental one. A similar conclusion can be drawn from the 3D DES computations with fixed transition model, which are actually giving rather good results in comparison to experimental ones for the whole range of angles of attack.

At $\alpha = 18^o$, all computational methods predict quite higher lift than the experiment. 3D RANS and DES computations with transition model, as well as 3D fully turbulent RANS predict lift levels that are between the extremely high values of the fully turbulent 3D DES and 2D RANS computations and the experimental

results.

Beyond $\alpha = 18^o$, all computational methods predict a distinct drop of lift and recover values somehow lower than the measurements for $\alpha = 20^o$.

Figs. 46(a-b-c) display the time-series of lift computed at angles of attack equal to $10, 14$ and 18^o, respectively. As it can be seen, the 2D RANS computational results are getting oscillatory with larger amplitude at the same time that the computed lift level increases with increasing angle of attack. Surprisingly, the 3D RANS computations are stationary for $\alpha = 18^o$.

The transition locations measured in the experiment, together with the one computed with the transition model by Drela [4] during 2D RANS calculations, are displayed in Fig. 45. It can be seen that there is a relative good agreement between these results. Both data sets show that the transition location on the suction side is very sensitive to the angle of attack around stall (i.e. for angles of attack between 6 and 8^o).

In the remaining of this section, the influence of 2D and 3D computations, the turbulence model, and the transition model are studied.

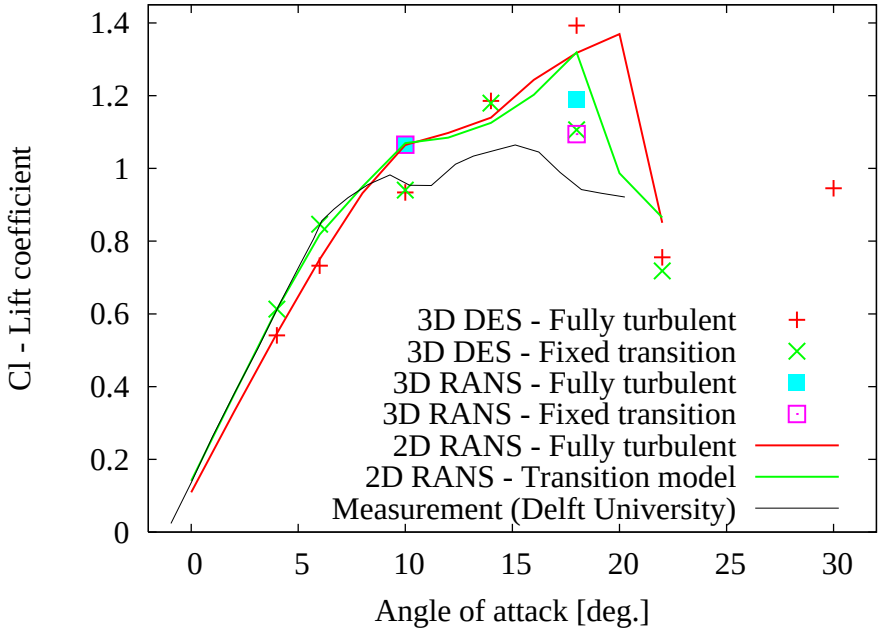

(a) Lift

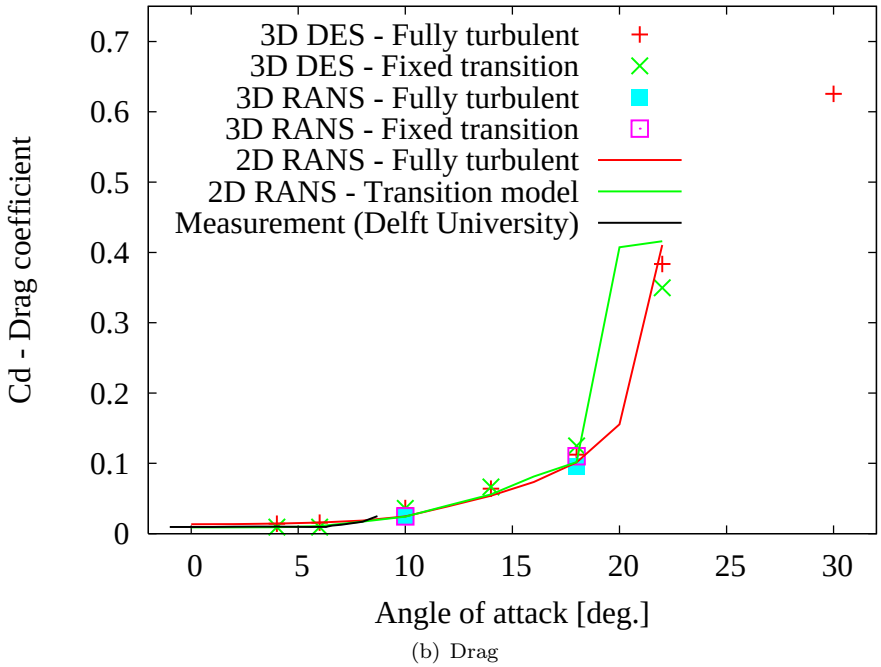

(b) Drag

Figure 44. Polar Characteristics for S809 Airfoil

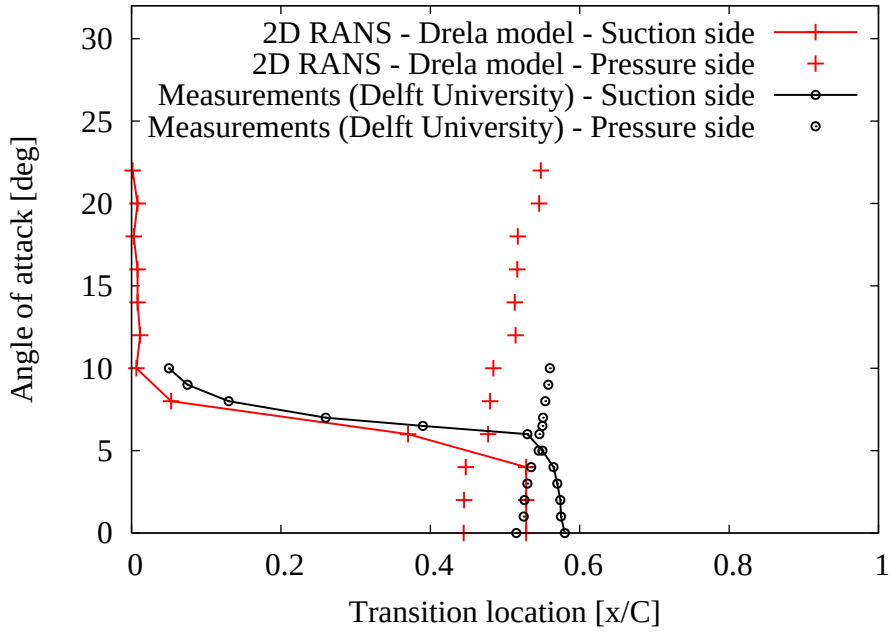

Figure 45. Transition Location for S809 Airfoil

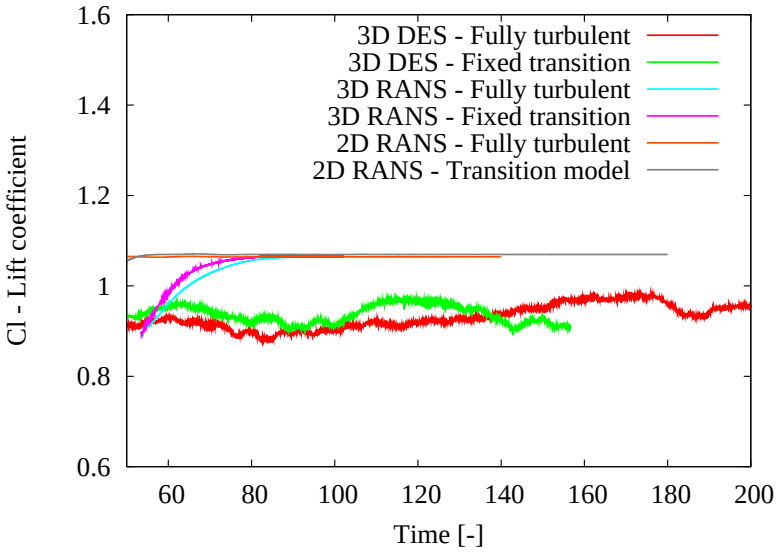

(a) $\alpha = 10^o$

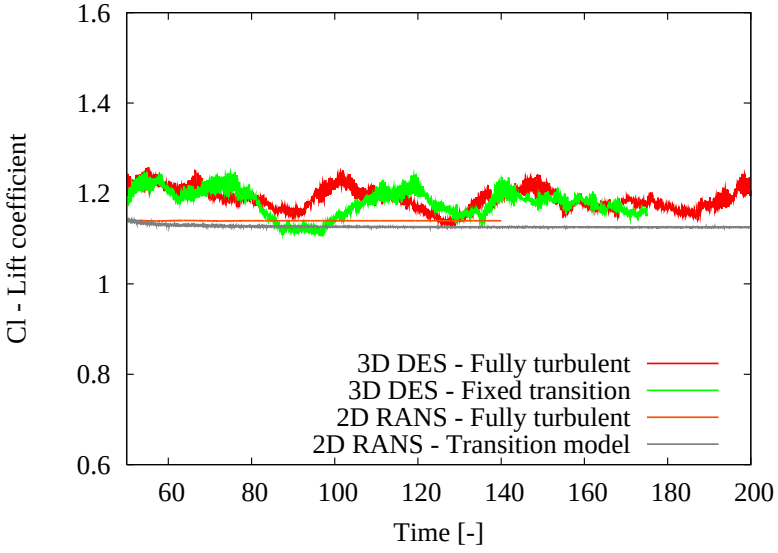

(b) $\alpha = 14^o$

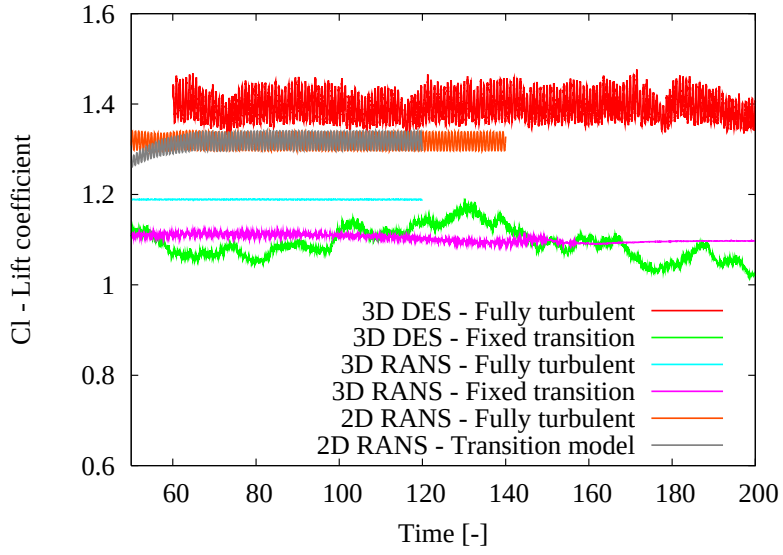

(c) $\alpha = 18^o$

Figure 46. Lift Time-Series for S809 Airfoil

Influence of the 2D/3D Computations and of the Turbulence Model

Polar characteristics are shown on Fig. 47 for fully turbulent computations. Figs. 48 and 49 display the pressure and skin friction coefficient distributions of fully turbulent computations for angles of attack equal to 10 and 18^o, respectively. Concerning the former one ($\alpha = 10^o$), it can be seen that the 2D and 3D RANS computations predict a smaller trailing edge separation than the 3D DES computation, which explains the differences in lift and drag levels in Fig. 47. At $\alpha = 18^o$ (Fig. 49), the small discrepancies between the different calculations induce a quite large difference in lift level as observed in Fig. 47(a). This is due to the fact that the pressure coefficient differences, even if relatively small to each other, involve high absolute values of this coefficient. Anyhow, recirculations lengths are similar for all calculations. At $\alpha = 22^o$, both 2D and 3D computations predict a completely separated flow as illustrated in Fig. 50, explaining the abrupt drop of lift and increase of drag.

Polar characteristics are shown on Fig. 51 for computations with transition model. Figs. 52 to 54 display the pressure and skin friction coefficient distributions computed with transition model for angles of attack equal to $10, 18$ and 22^o, respectively. Again, at $\alpha = 10^o$, the 2D and 3D RANS calculations predict a smaller trailing edge separation than the 3D DES calculation. At $\alpha = 18^o$, both 3D RANS and 3D DES gives similar results in average, although the DES computation is more three-dimensional and chaotic along the airfoil span. At $\alpha = 22^o$, both 2D and 3D computations predict a completely separated flow. For $\alpha = 18$ and 22^o, the three-dimensional chaotic structures of the 3D computations seem to be responsible for the lower pressure coefficient distribution on the suction side, and thereby the lower lift level observed in Fig. 51.

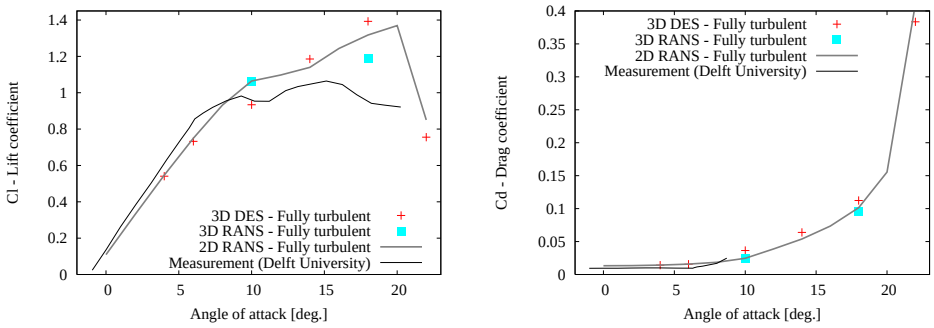

(a) Lift (b) Drag

Figure 47. Polar Characteristics - S809 Airfoil - Fully Turbulent Computations

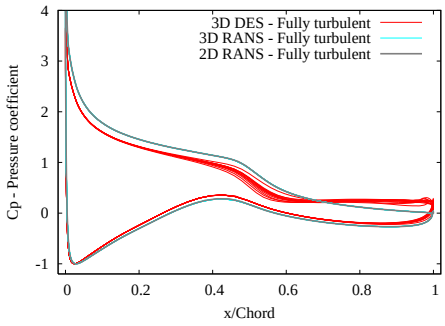

(a) Pressure Distribution - $\alpha = 10^o$

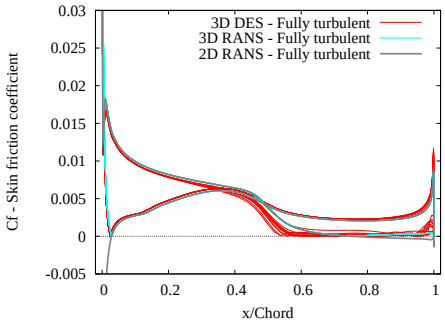

(b) Skin Friction Distribution - $\alpha = 10^o$

Figure 48. C_p and C_f Distributions - S809 Airfoil - Fully Turbulent - $\alpha = 10^o$

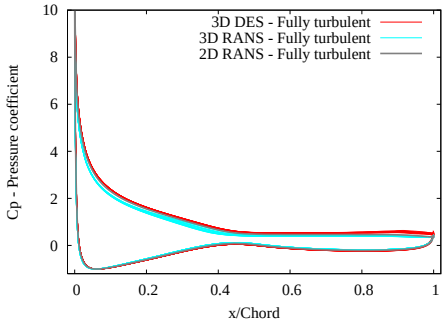

(a) Pressure Distribution - $\alpha = 18^o$

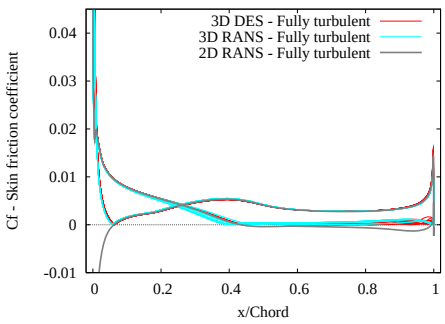

(b) Skin Friction Distribution - $\alpha = 18^o$

Figure 49. C_p and C_f Distributions - S809 Airfoil - Fully Turbulent - $\alpha = 18^o$

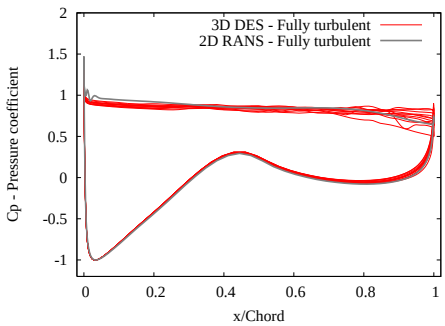

(a) Pressure Distribution - $\alpha = 22^o$

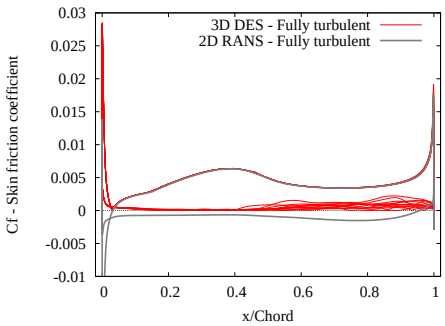

(b) Skin Friction Distribution - $\alpha = 22^o$

Figure 50. C_p and C_f Distributions - S809 Airfoil - Fully Turbulent - $\alpha = 22^o$

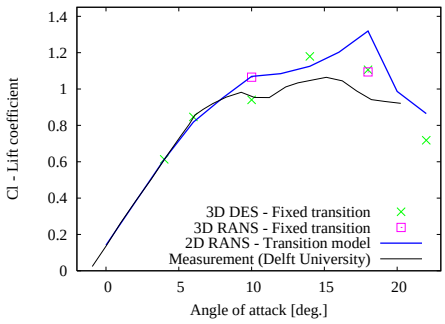

(a) Lift

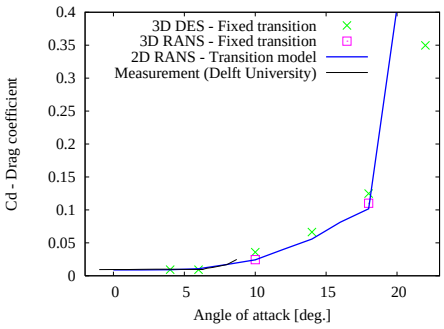

(b) Drag

Figure 51. Polar Characteristics - S809 Airfoil - With Transition Model

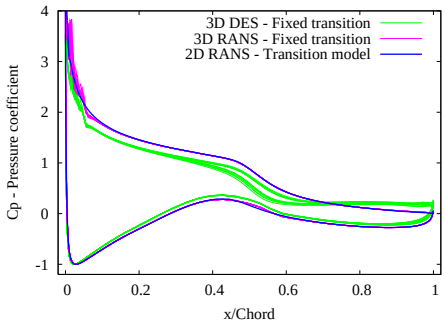

(a) Pressure Distribution - $\alpha = 10^o$

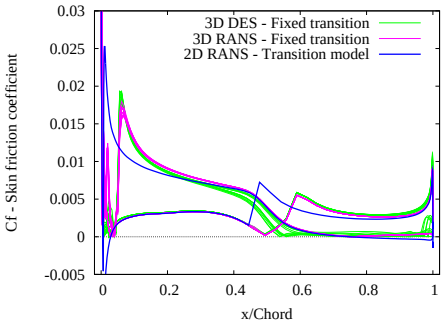

(b) Skin Friction Distribution - $\alpha = 10^o$

Figure 52. C_p and C_f Distributions - S809 Airfoil - Transition Model - $\alpha = 10^o$

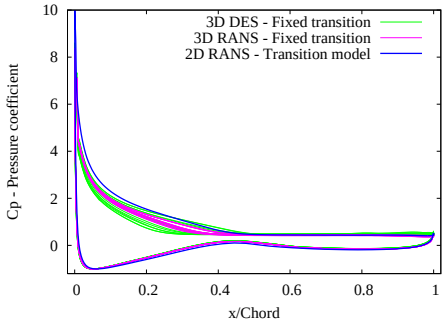

(a) Pressure Distribution - $\alpha = 18^o$

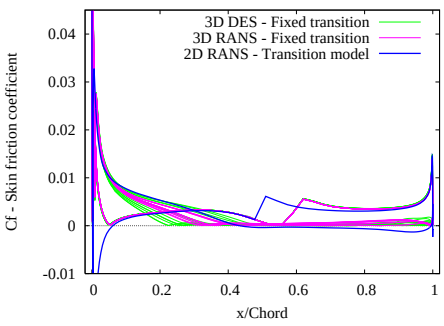

(b) Skin Friction Distribution - $\alpha = 18^o$

Figure 53. C_p and C_f Distributions - S809 Airfoil - Transition Model - $\alpha = 18^o$

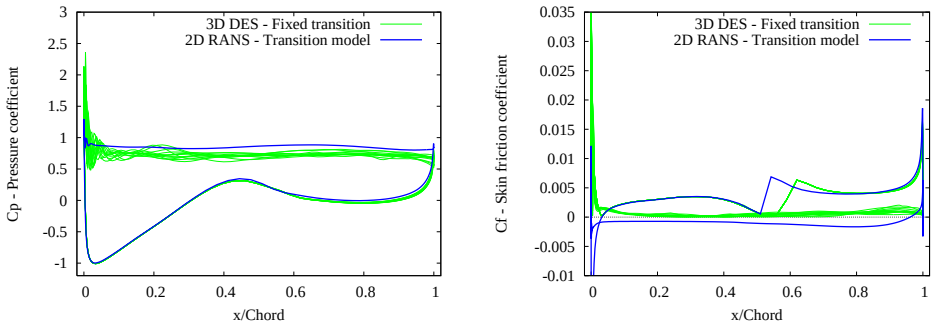

(a) Pressure Distribution - $\alpha = 22^o$ (b) Skin Friction Distribution - $\alpha = 22^o$

Figure 54. C_p and C_f Distributions - S809 Airfoil - Transition Model - $\alpha = 22^o$

Effect of the Transition Model

As illustrated in Fig. 45, the transition locations measured in the experiment [20] are in relative good agreement with the ones obtained with the transition model by Drela [4] implemented in the 2D RANS calculations [13]. Remind that in the 3D calculations with fixed transition, the transition location is extracted from the experimental data up to $\alpha = 10^o$ (see section 6.1). However, if the transition location would have been extracted from 2D calculations with Drela's model, one could expect that the computed results would be very similar as both sets of data are quite close to each other, as mentioned above.

Polar characteristics are shown in Fig. 55. On Figs. 56 to 60, the pressure and skin friction coefficient distributions at several station across the airfoil span are plotted for angles of attack equal to $4, 10, 18$ and 22^o, respectively. At $\alpha = 4^o$, the influence of the transition can clearly be seen on the skin friction. Indeed, in the 3D fully turbulent DES the boundary layer is much thicker on the suction side of the aifoil near the leading edge, inducing a slightly smaller pressure coefficient on this part of the airfoil and resulting in a lower lift and higher drag (as described in section 5.2, p.35). As for the 3D DES computation with transition, transition occurs rather far from the leading edge (at $x/C = 0.565$, see Fig. 45). Therefore, a laminar separation is able to occur at approximately $x/C = 0.45$, and reattachement apparently occurs before transition. However, downstream of this point, both fully turbulent computation and computation with transition exhibit similar pressure coefficients.

At $\alpha = 10^o$ (see Fig. 57), transition location on the suction side has moved noticeably forward and occurs now close to the leading edge. Therefore, fully turbulent computational results are in good agreement with the computations with transition model.

More interesting is what happens for $\alpha = 18^o$ (see Fig. 58). In this case, the transition location was extracted from 2D RANS calculations with the transition model by Drela (as it was not available from experimental results [20]). The transition location on the suction side was set to $x/C = 0.006$, and $x/C = 0.6$ on the pressure side. Even if the suction side transition location if very close to the leading edge, the physics of the flow is quite different from the fully turbulent case. Indeed, as it can be seen on a close-up of the skin friction coefficient in the vicinity of the leading edge (Fig. 61(b)), the fixed transition computation allows the formation of a laminar recirculation bubble (between $x/c = 0.002$ and 0.006) before transition is effective. Reattachment occurs near the transition location, and for $x/C \approx 0.03$, the skin friction coefficient momentarily recovers values similar to the fully turbulent case. However, as can be seen on Fig. 58, this laminar separation bubble causes chaotic patterns along the span of the blade, which make the flow more three-dimensional compared to the fully turbulent case. This conclusion is confirmed by comparing the isovalues of the pressure and vorticity on Figs. 62 and 63. As a consequence, fully turbulent computation predicts a noticeably higher lift than the one with transition model for this specific angle of attack (see Fig. 55(a)).

Finally, at an angle of attack of $\alpha = 22^o$ (see Fig. 60), both for fully turbulent 3D DES computation and the one with transition model, detachment clearly occurs on the whole suction side of the airfoil inducing an important drop of lift and increase of drag for both cases as observed on Fig. 55.

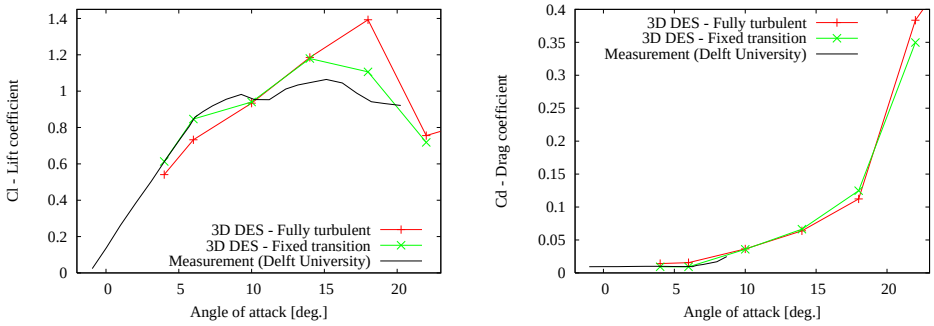

(a) Lift (b) Drag

Figure 55. Polar Characteristics - S809 Airfoil - DES Computations - Influence of Transition

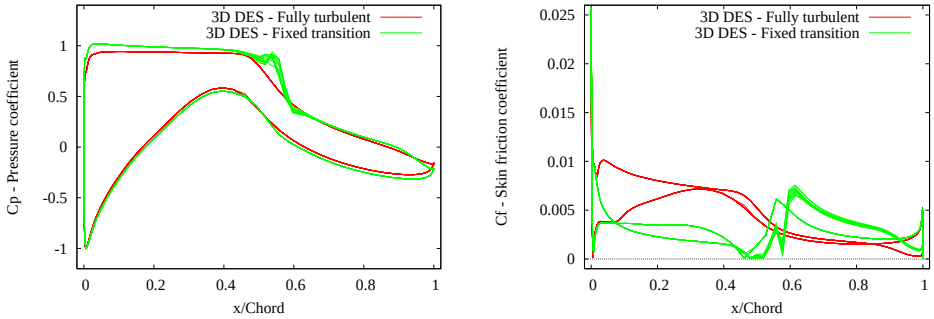

(a) Pressure Distribution - $\alpha = 04^o$ (b) Skin Friction Distribution - $\alpha = 04^o$

Figure 56. C_p and C_f Distributions - S809 Airfoil - DES Computations - $\alpha = 04^o$

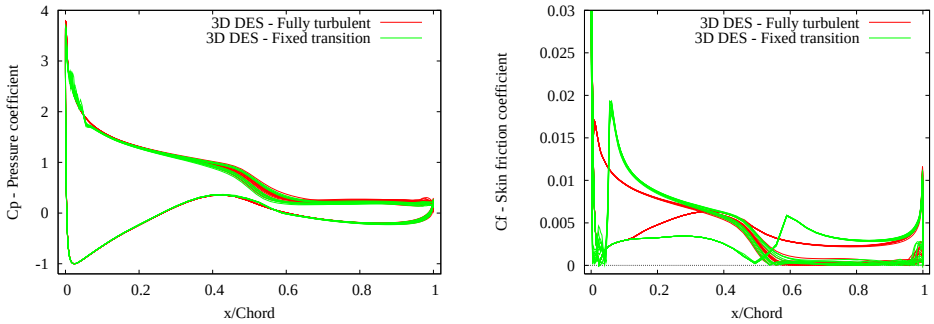

(a) Pressure Distribution - $\alpha = 10^o$ (b) Skin Friction Distribution - $\alpha = 10^o$

Figure 57. C_p and C_f Distributions - S809 Airfoil - DES Computations - $\alpha = 10^o$

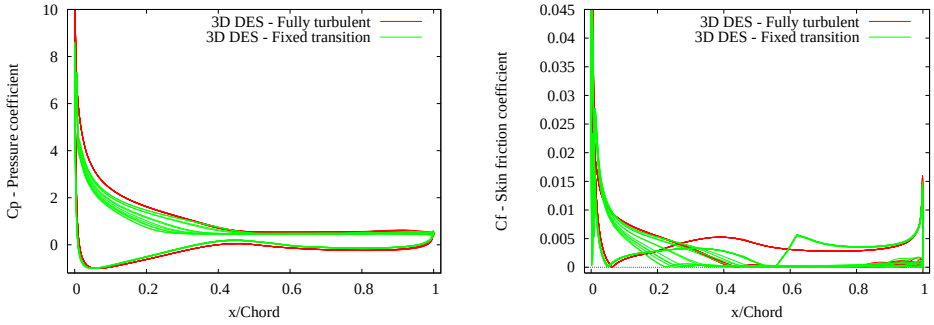

(a) Pressure Distribution - $\alpha = 18^o$ (b) Skin Friction Distribution - $\alpha = 18^o$

Figure 58. C_p and C_f Distributions - S809 Airfoil - DES Computations - $\alpha = 18^o$

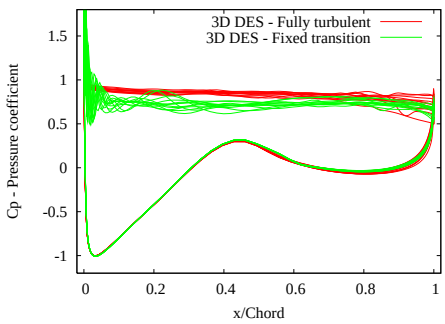

(a) Pressure Distribution - $\alpha = 22^o$

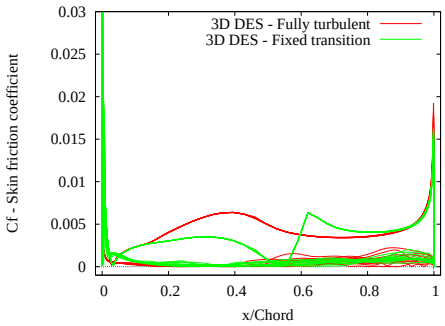

(b) Skin Friction Distribution - $\alpha = 22^o$

Figure 59. C_p and C_f Distributions - S809 Airfoil - DES Computations - $\alpha = 22^o$

Figure 60. S809 Airfoil at $\alpha = 22^o$ - DES Computations - Influence of Transition

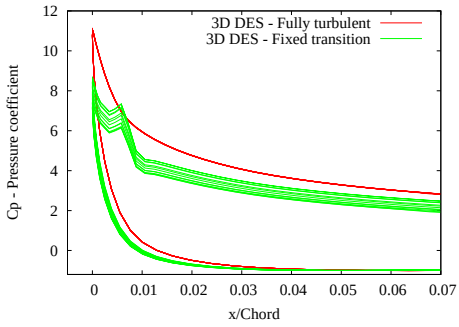

(a) Pressure Distribution - $\alpha = 18^o$

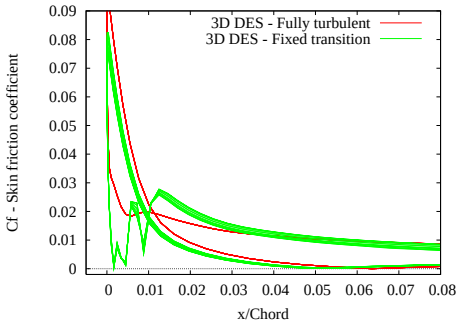

(b) Skin Friction Distribution - $\alpha = 18^o$

Figure 61. C_p and C_f Distributions - S809 Airfoil - DES Computations - $\alpha = 18^o$ (Close-up of leading edge)

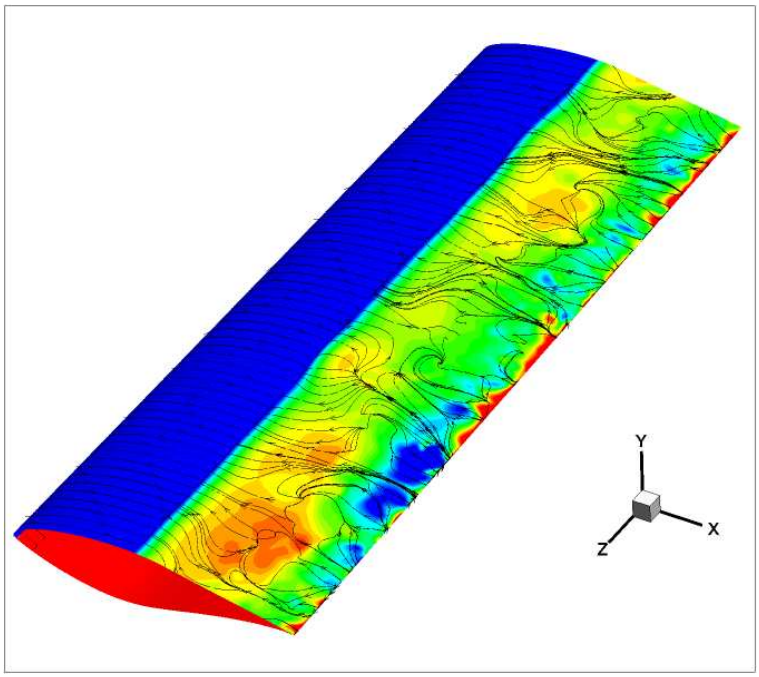

(a) Surface Iso-Pressure and Limiting Streamlines

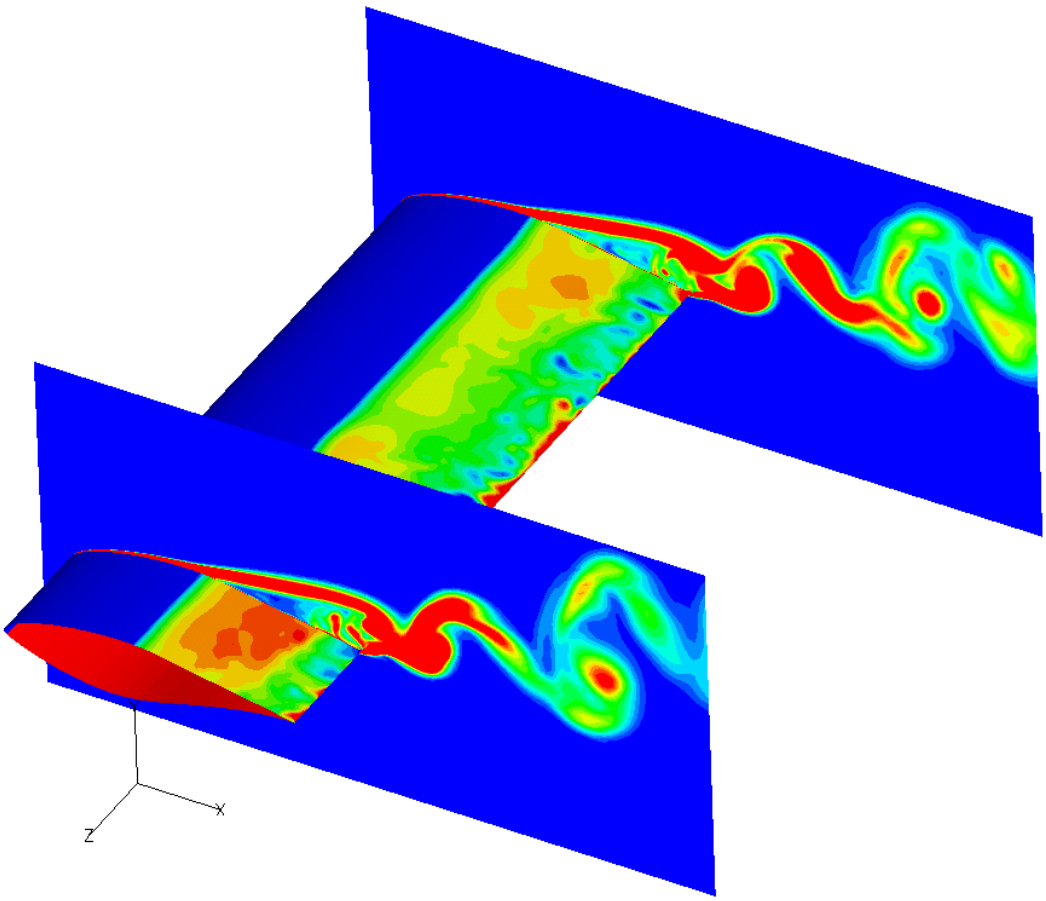

(b) Surface Pressure Isovalues, and Cross-Section Vorticity Isovalues

Figure 62. S809 Airfoil at $\alpha = 18^o$ - 3D DES - Fully Turbulent

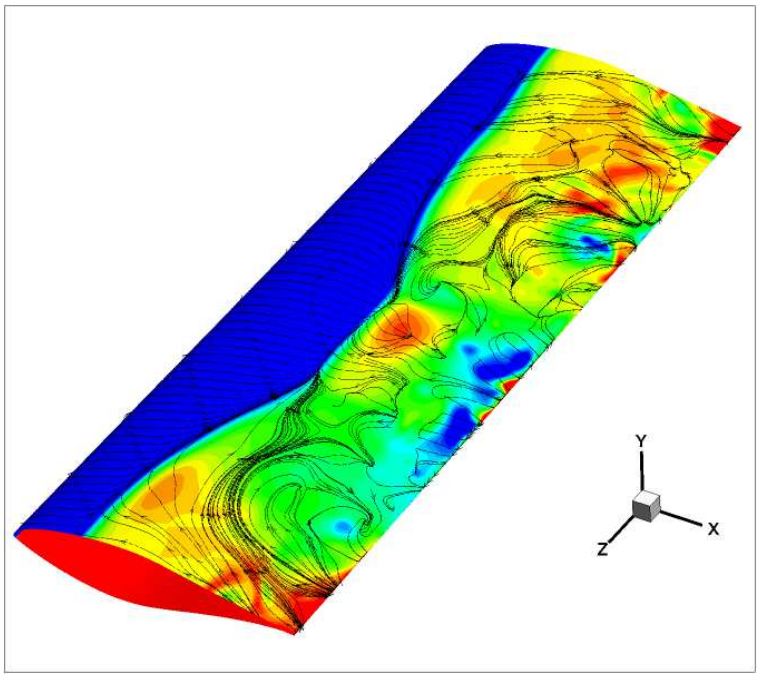

(a) Surface Iso-Pressure and Limiting Streamlines

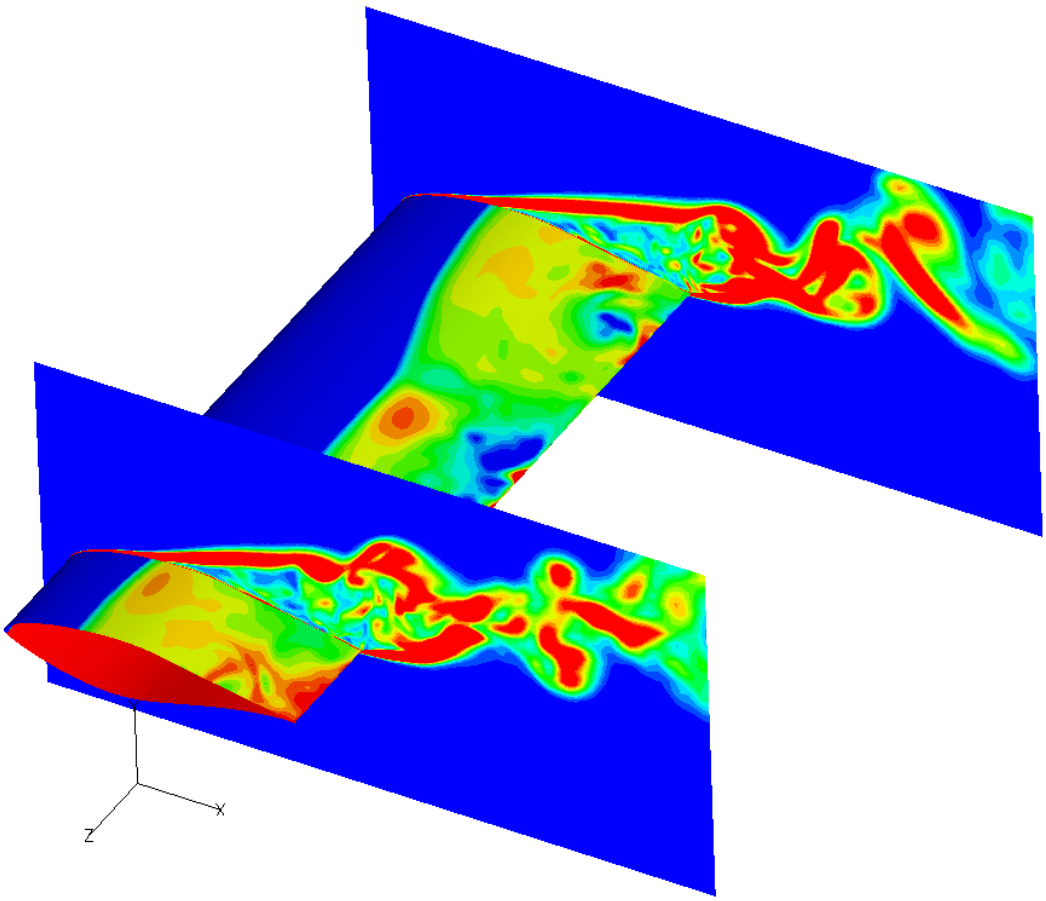

(b) Surface Pressure Isovalues, and Cross-Section Vorticity Isovalues

Figure 63. S809 Airfoil at $\alpha = 18^o$ - 3D DES - Fixed Transition

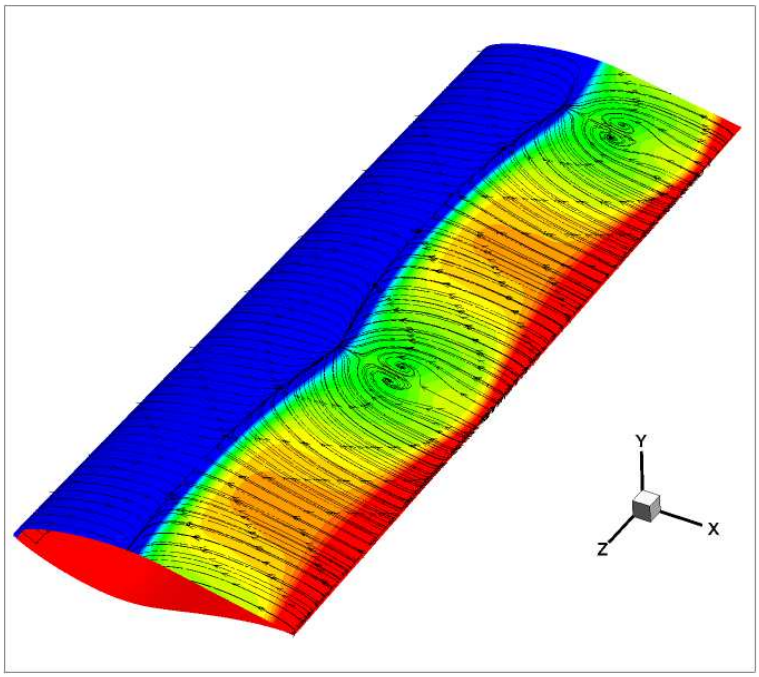

(a) Surface Iso-Pressure and Limiting Streamlines

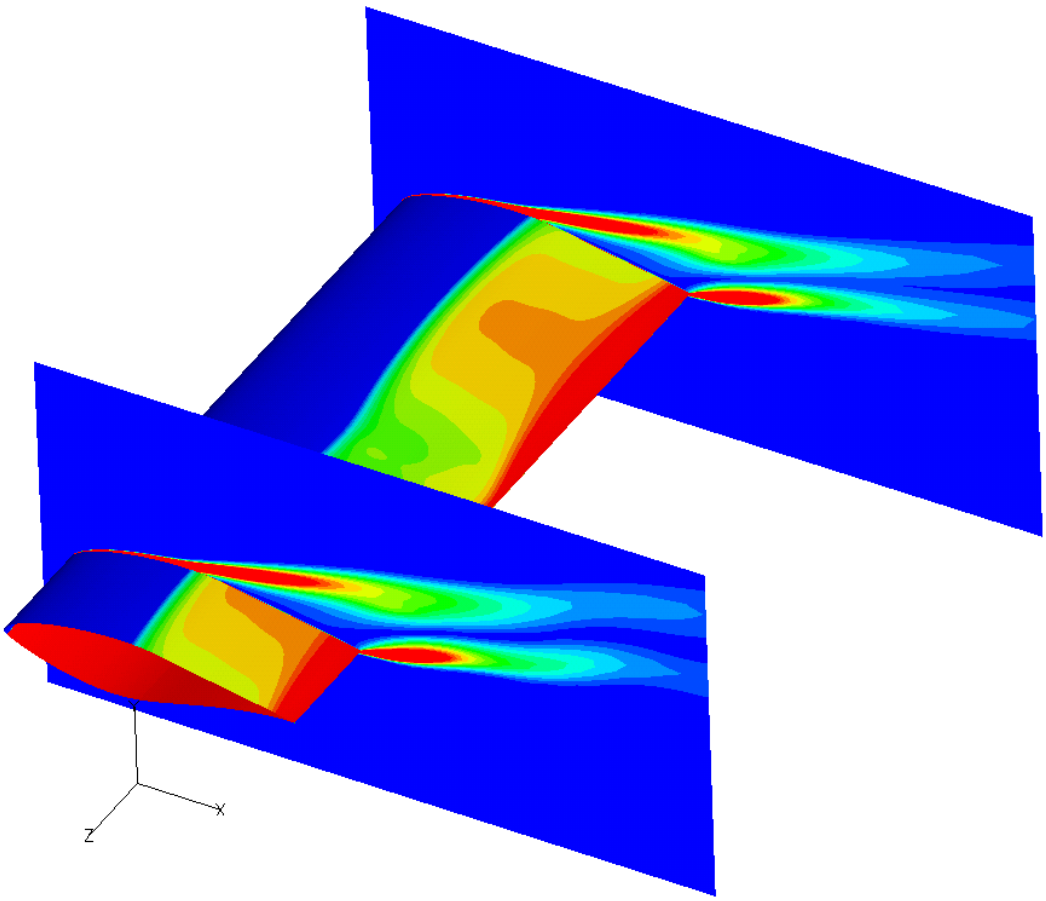

(b) Surface Pressure Isovalues, and Cross-Section Vorticity Isovalues

Figure 64. S809 Airfoil at $\alpha = 18^o$ - 3D RANS - Fully Turbulent

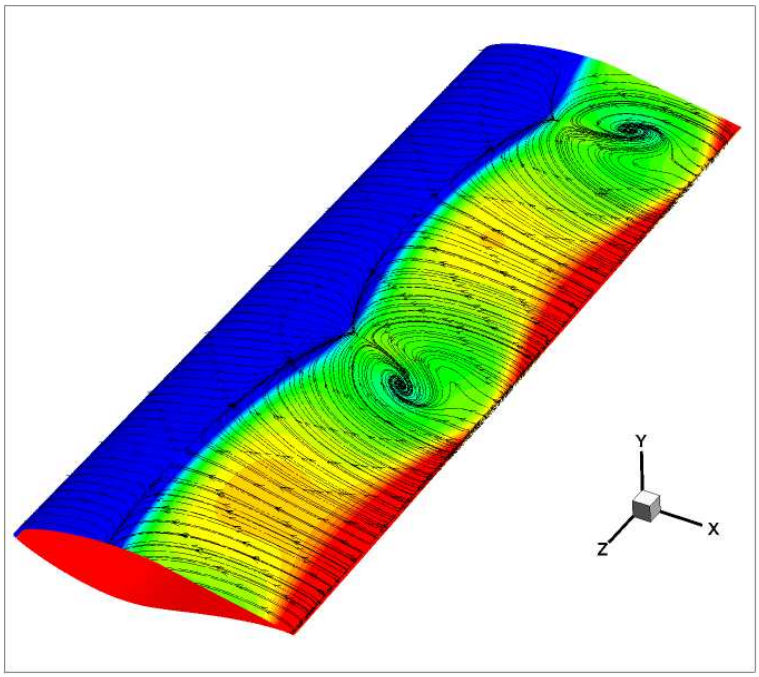

(a) Surface Iso-Pressure and Limiting Streamlines

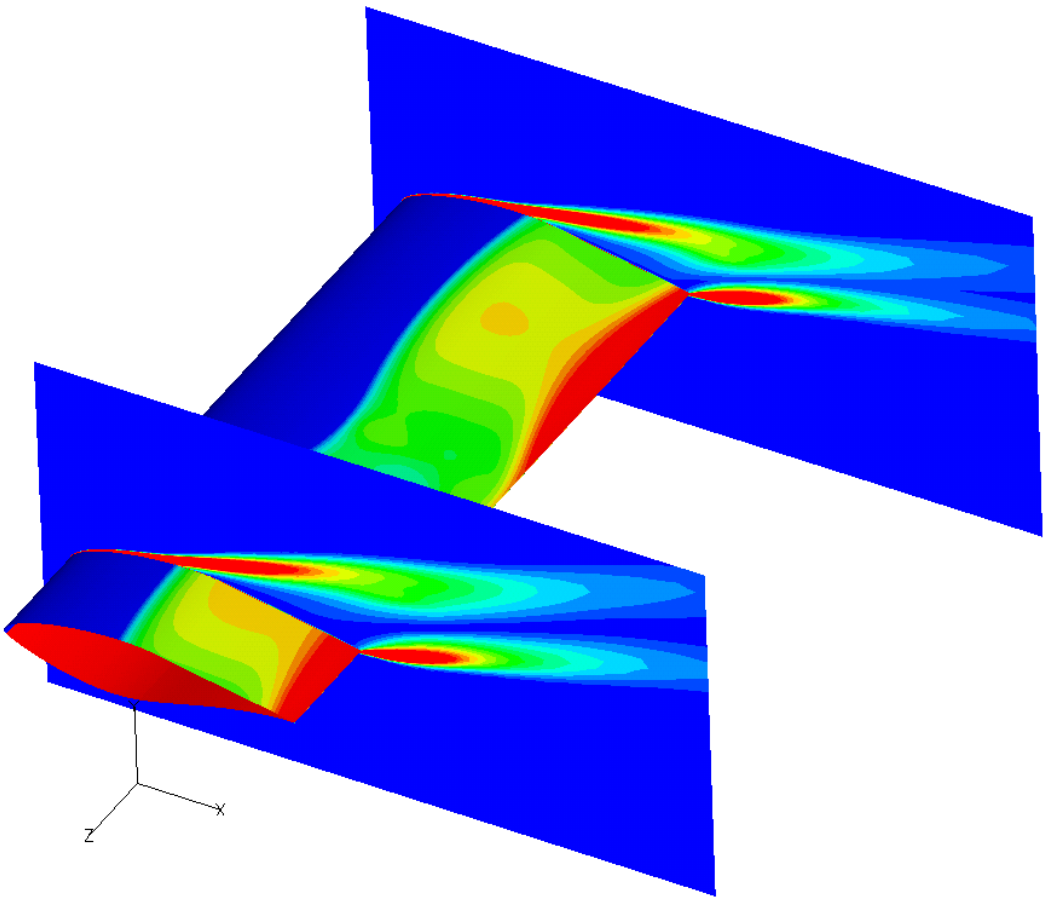

(b) Surface Pressure Isovalues, and Cross-Section Vorticity Isovalues

Figure 65. S809 Airfoil at $\alpha = 18^o$ - 3D RANS - Fixed Transition

6.3 Summary of Results

According to the computational results, this airfoil is sensitive to transition both in the linear and in the stall region. It is clear that DES modelling is necessary to accurately predict stall occurrence. Some discrepancies with the experimental results are observed after stall and before full separation of the flow on the suction side. Indeed, all computational methods predict a too high increase of lift as the angle of attack increases in this region. Transition modelling seems to improve the results in this case. Moreover, the 3D computations perform better than the 2D ones, except for the fully turbulent 3D DES calculation just before full separation of the flow. The 3D DES computations with transition model are performing quite well compared to experimental results.

7 Results for the DU 93-W-210 Airfoil

This section is concerned with the 21% thick wind turbine airfoil DU 93-W-210 which was designed by W.A. Timmer [23] from Delft University. It was tested in the low-speed low-turbulence wind tunnel of the Faculty of Aerospace Engineering at Delft University [24]. Measurements were performed at a Reynolds number equal to 1.0×10^6. The experimental results were made available to the authors by Delft University, but were not published in the litterature.

7.1 Test cases

The computations were all performed with the DES turbulence model. Three configurations were studied: the fully turbulent configuration, the fixed transition model for which the transition location was extracted from 2D calculations with the transition model by Drela [4] implemented as described in [13], and finally the simplified transition model as described in section 2.2. These results are compared to measurement data, as well as computational results with the 2D RANS solver EllipSys2D, both in the fully turbulent case and with the transition model by Drela.

7.2 Results

Lift and drag characteristics for all cases are gathered in Figs. 66(a-b). It is clear that computations with transition model give results in better agreement with measurements before stall, and a marginal improvement after stall. However, it seems that all computations predict a continued growth of lift after stall (for $\alpha > 14^o$), whereas experimental results exhibit a nearly constant drag after stall. However, the 3D DES computation predicts a distinct drop of lift for $\alpha = 24^o$. Drag is quite well predicted by computational methods, except for the fully turbulent computations (as it was observed for the lift), and around stall.

The transition locations as a function of the angle of attack predicted by the 2D RANS computations with the model by Drela, together with the results of the simplified transition model in the 3D DES calculations, are plotted on Fig. 67. A discussion on the discrepancies between the transition locations predicted by the simplified transition model and the 2D RANS computations is available in section 5.2.

In this section, the influence of the transition model on the 3D DES computations is investigated, followed by a comparison of the 2D and 3D results.

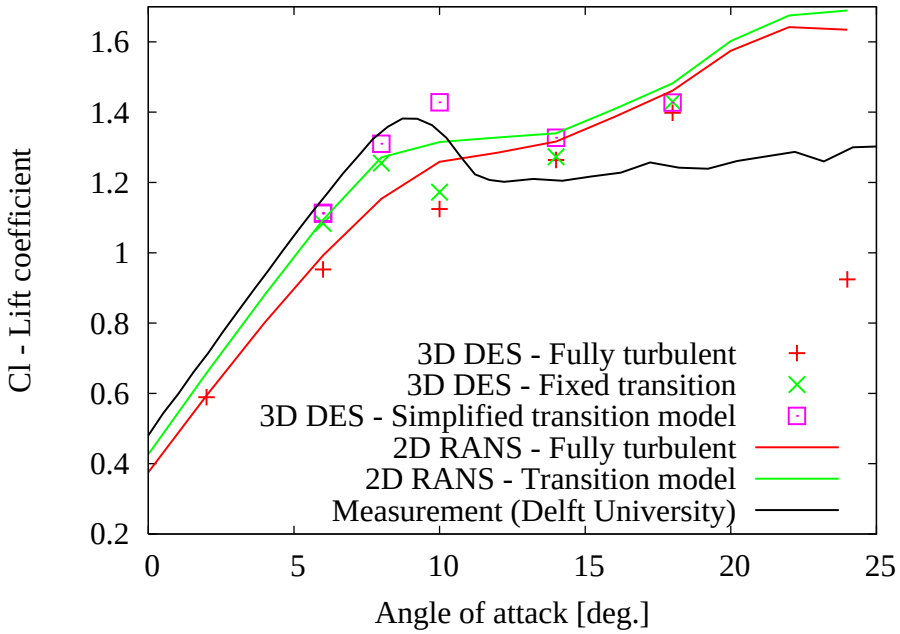

(a) Lift

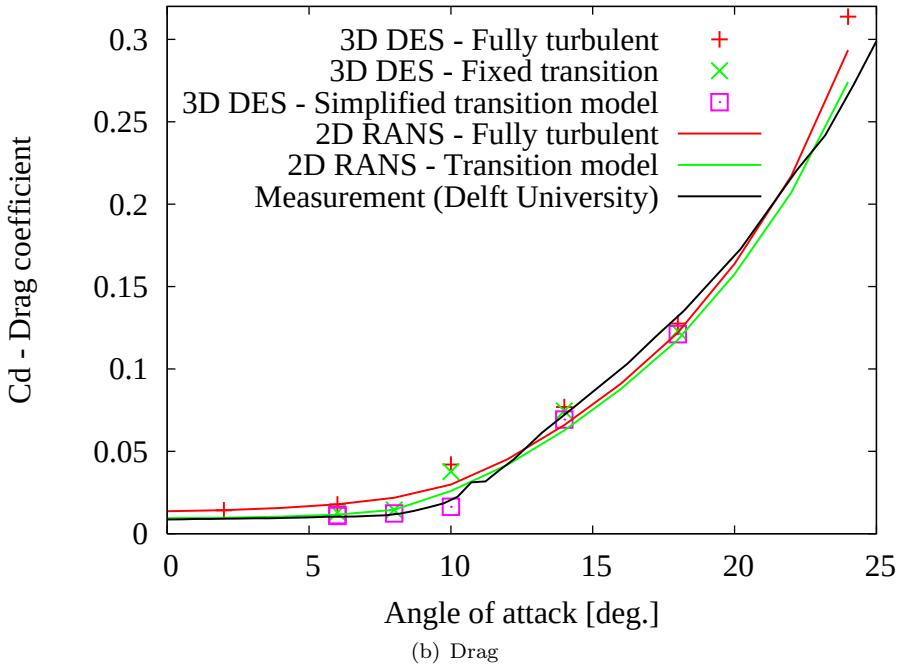

(b) Drag

Figure 66. Polar Characteristics for DU 93-W-210 Airfoil

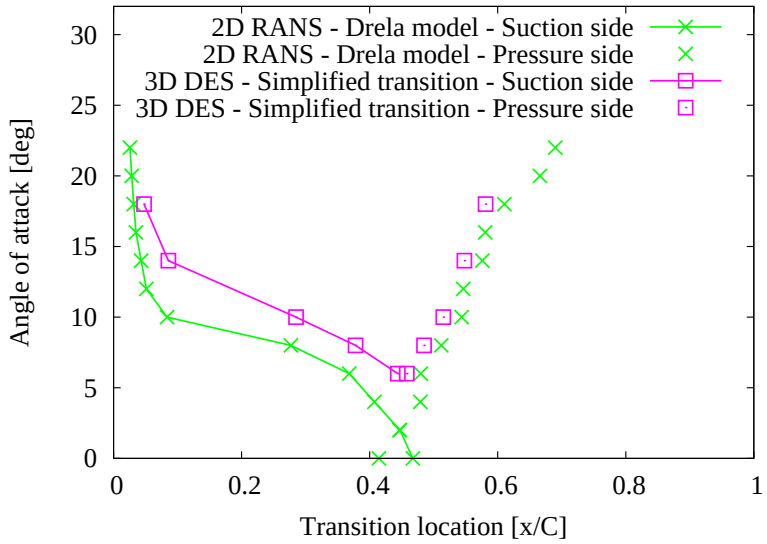

Figure 67. Transition Location for DU 93-W2-10 Airfoil

Effect of the Transition Model

Lift and drag characteristics for the 3D DES computations are compared with measurement data on Fig. 68. Pressure and skin friction coefficient distributions at angles of attack equal to $6, 10, 14$ and 18^o are displayed in Figs. 69 to 72, respectively.

It is clear that the 3D DES computations in the fully turbulent configuration exhibit a too low lift and too high drag before stall. It can be seen from the pressure and skin friction coefficients that the thick turbulent boundary layer downstream the leading edge on the suction side induces a lower pressure coefficient (as described in section 5.2, p.35) on this part of the airfoil for $\alpha = 6$ and 10^o, in Figs. 69 and 70) respectively, resulting in the above-mentioned discrepancies. Computations with both fixed and simplified transition models are in quite good agreement with the experimental results for $\alpha = 6$ and 8^o.

Beyond stall ($\alpha = 14$ and 18^o, Figs. 71 and 72), all computational results are quite similar to each other as can be seen both on the polar characteristics, and the pressure and skin friction distributions. However, they all predict a new lift increase after $\alpha = 14^o$, whereas the measured lift remain quite constant and at a lower level after the lift drop due to stall (which might be caused by wind tunnel effects). Nevertheless, the computed drag is close to the experimental one.

It is interesting to note that the fixed transition model and the simplified transition model behave very differently around stall, i.e. for $\alpha = 10^o$. The only difference between the two models is the fact that the simplified transition model uses the stagnation point to determine the transition location. Indeed, it can be seen both on Fig. 70(b), and from the transition location on Fig. 67, that transition occurs much closer to the leading edge for the computation with fixed transition model (the 2D RANS transition location being the one enforced in the 3D DES computation with fixed transition). This results in a trailing edge separation for the computation with fixed transition model, which does not occur with the simplified transition model, explaining the earlier stall for the computations with fixed transition model observed on Fig. 68.

The transition location along the span of the airfoil predicted by the simplified transition model is compared with the fixed transition location on Fig. 73 for various angles of attack. It can be seen that there is not much variation of the predicted transition location along the span of the airfoil, but quite large differences between the two models, especially around stall ($\alpha = 8$ and 10^o) as it can be expected since the transition location is very sensitive to the angle of attack in this area (as seen on Fig. 67).

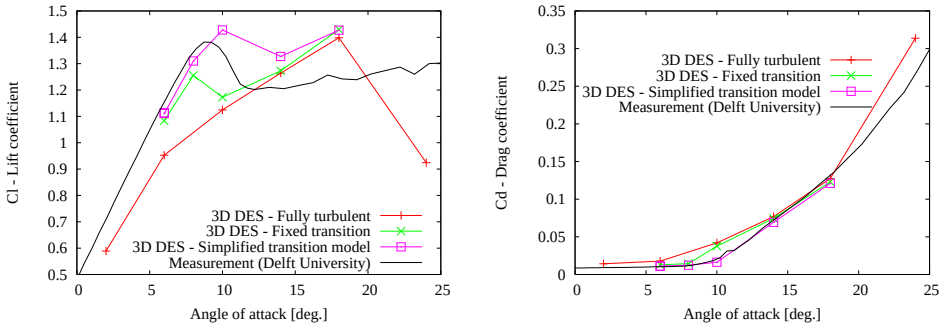

(a) Lift (b) Drag

Figure 68. Polar Characteristics - DU 93-W-210 Airfoil - 3D DES Computations - Influence of Transition

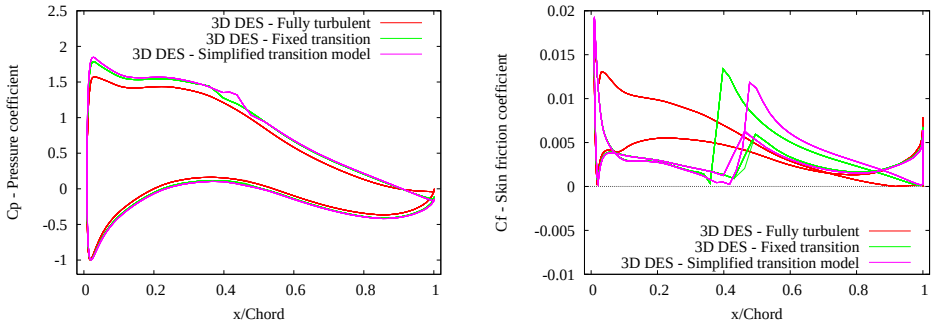

(a) Pressure Distribution - $\alpha = 06^o$ (b) Skin Friction Distribution - $\alpha = 06^o$

Figure 69. C_p and C_f Distributions - DU 93-W-210 - 3D DES Computations - $\alpha = 06^o$

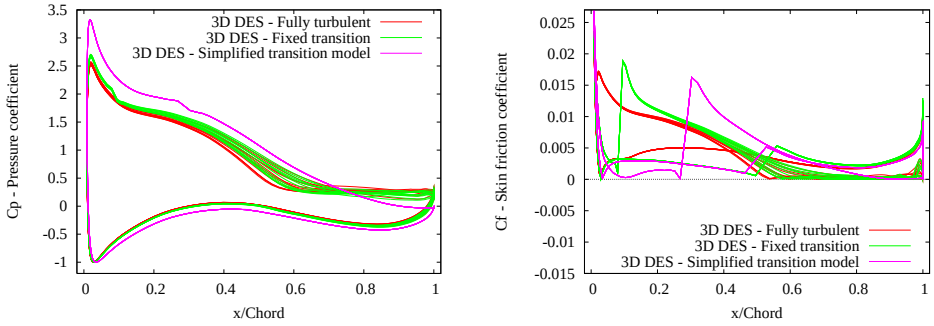

(a) Pressure Distribution - $\alpha = 10^o$ (b) Skin Friction Distribution - $\alpha = 10^o$

Figure 70. C_p and C_f Distributions - DU 93-W-210 - 3D DES Computations - $\alpha = 10^o$

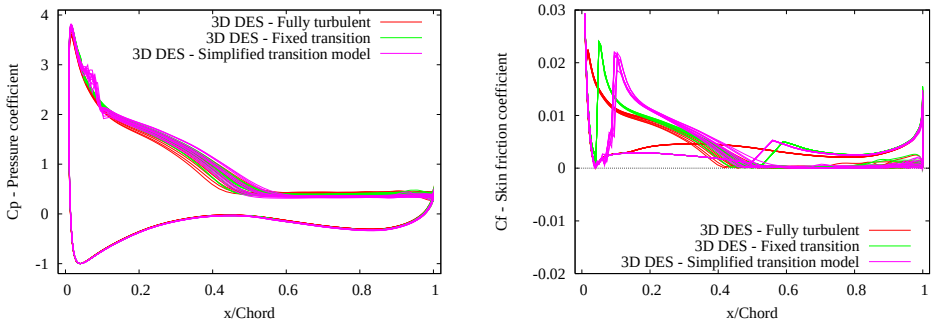

(a) Pressure Distribution - $\alpha = 14^o$ (b) Skin Friction Distribution - $\alpha = 14^o$

Figure 71. C_p and C_f Distributions - DU 93-W-210 - 3D DES Computations - $\alpha = 14^o$

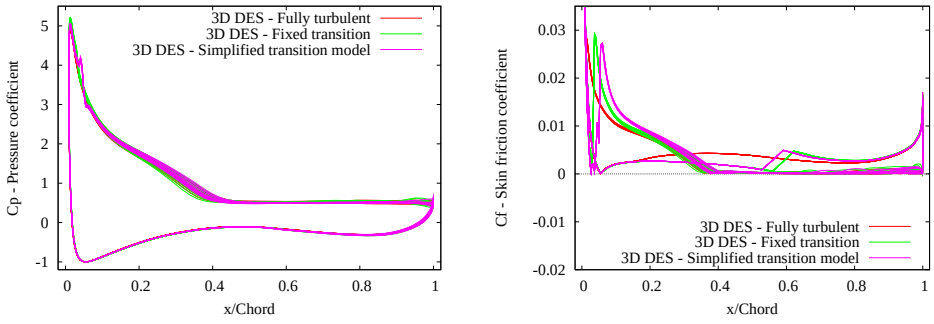

(a) Pressure Distribution - $\alpha = 18^o$ (b) Skin Friction Distribution - $\alpha = 18^o$

Figure 72. C_p and C_f Distributions - DU 93-W-210 - 3D DES Computations - $\alpha = 18^o$

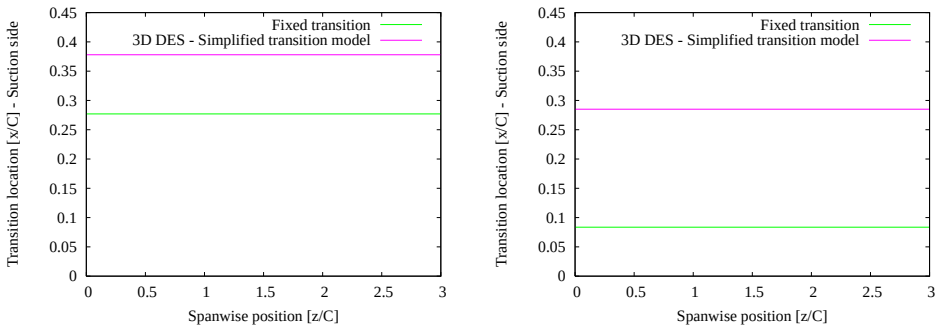

(a) $\alpha = 08^o$ (b) $\alpha = 10^o$

(c) $\alpha = 14^o$ (d) $\alpha = 18^o$

Figure 73. Transition Location along Span on Suction Side - DU 93-W-210 Airfoil

Comparison 2D/3D

In this section, 2D RANS and 3D DES computations, both with and without transition model, are compared with experimental results. In the case of the 3D computations, the fixed transition model is used.

Lift and drag characteristics are displayed on Fig. 74. Pressure and skin friction coefficient distributions at angles of attack equal to $6, 10, 14$ and 24^o are displayed in Figs. 75 to 78, respectively. Conclusions are quite similar to the previous section. Indeed, computed results obtained with a transition model are in good agreement with measurements before stall. All computed results exhibit a continued increase of lift beyond stall which does not occur in the measurements, whereas the drag level is quite close predicted. However, the 2D computations are closer to the experimental results around stall as shown in Fig. 74. At $\alpha = 24^o$ (Fig. 78), it can be seen that the 3D DES computation is detached almost everywhere on the suction side of the airfoil explaining the drop of lift in Fig. 74 for that angle of attack, whereas 2D computations only predict a detachment starting around the 1/4 chord.

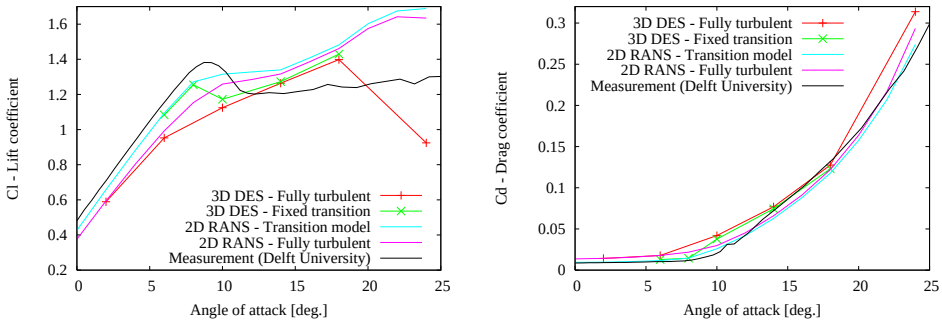

(a) Lift (b) Drag

Figure 74. Polar Characteristics - DU 93-W-210 - Comparison 2D RANS/3D DES

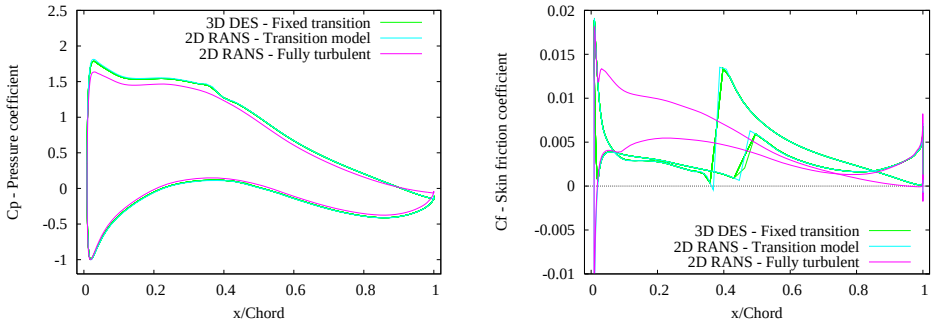

(a) Pressure Distribution - $\alpha = 06^o$ (b) Skin Friction Distribution - $\alpha = 06^o$

Figure 75. C_p and C_f Distributions - DU 93-W-210 Airfoil - $\alpha = 06^o$

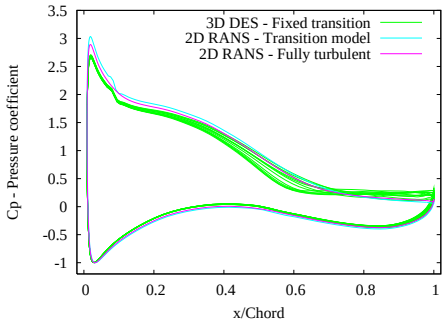

(a) Pressure Distribution - $\alpha = 10^o$

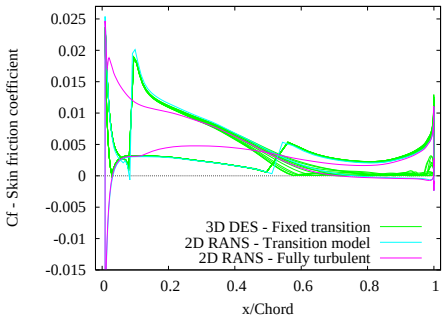

(b) Skin Friction Distribution - $\alpha = 10^o$

Figure 76. C_p and C_f Distributions - DU 93-W-210 Airfoil - $\alpha = 10^o$

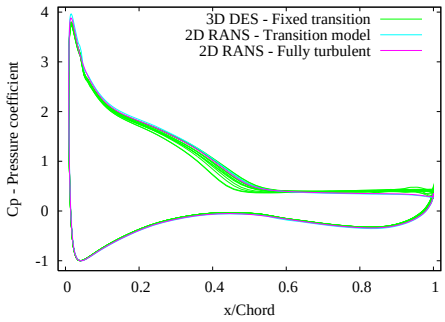

(a) Pressure Distribution - $\alpha = 14^o$

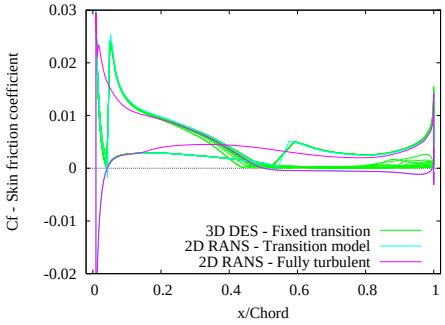

(b) Skin Friction Distribution - $\alpha = 14^o$

Figure 77. C_p and C_f Distributions - DU 93-W-210 Airfoil - $\alpha = 14^o$

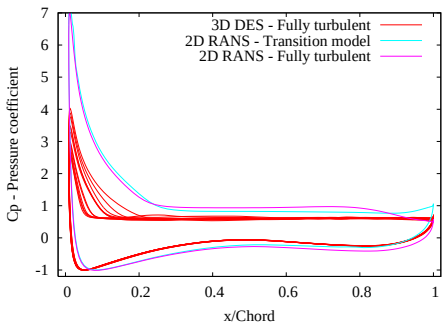

(a) Pressure Distribution - $\alpha = 24^o$

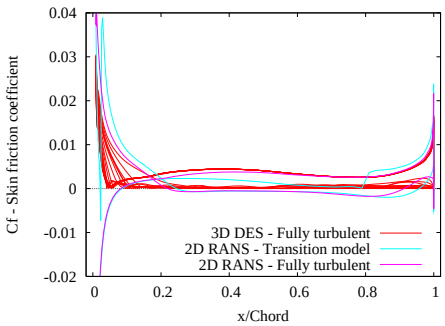

(b) Skin Friction Distribution - $\alpha = 24^o$

Figure 78. C_p and C_f Distributions - DU 93-W-210 Airfoil - $\alpha = 24^o$

7.3 Summary of Results

According to the computational results, this airfoil is sensitive to transition in the linear region and around stall, but in a lesser degree beyond stall. The same phenomenon of continued lift increase after stall is occurring again as observed for the S809 airfoil (see section6.2). 3D computations are necessary to simulate the three-dimensional chaotic structures present at high angles of attack.

8 Analysis of the Results

In this section, it is attempted to make a synthesis of the results obtained for the different airfoils. Considering the rather large amount of data, and the many conclusions that can be drawn for general and particular cases, the results will be classified in a two-entry array fashion. On one side, the results will be interpreted according to the ranges of angle of attack that characterize different types of flow conditions:

- *Linear region*, i.e. angles of attack for which the lift slope is nearly constant (at least according to potential theory), and nearly constant drag.
- *Around stall*, i.e. for angles of attack immediately preceding stall occurrence as well as immediately following.
- *Stall region*, i.e. angles of attack for which stall has already occurred, usually characterized by a rather constant lift but rapidly increasing drag.
- *Deep stall*, i.e. higher angles of attack relatively far from stall occurrence for which the flow over the airfoil suction side is completely detached.

The second parameter for our classification will be the comparison of results according to the physical models that are used for the computations. The following comparisons are performed:

- Comparison between 2D and 3D computations
- Comparison of RANS and DES computations
- Influence of transition modelling

Note that in these comparisons, the experimental results will be taken to a certain extent as a reference, but it is important to keep in mind that in this study we are actually more interested in the analysis of the different numerical and physical models relatively to each other (i.e. 2D vs. 3D computations, RANS vs. DES, and fully turbulent vs. transition modelling).

The conclusions that will be drawn in the following are not always general, and cannot be taken for granted for all types of airfoils. Indeed, the four different airfoils that are studied in this work are quite different from each other insofar as they exhibit quite different behaviors.

8.1 Linear Region

Comparison 2D/3D

3D effects are usually not relevant, except for thick airfoils (such as the NACA 63-430 airfoil, which anyway does not exhibit a distinct linear region before stall. In particular, trailing edge separation and unsteady effects are already present for low angles of attack).

Comparison RANS/DES

There is a low sensitivity to RANS/DES computational models, as the LES component of the DES model is not active in this case.

Influence of Transition

Transition is usually decisive for the prediction of lift slope. However, airfoils which are designed to be transition-insensitive (such as the RISØ-B1-18 airfoil) do not follow this rule.

8.2 Around Stall

Comparison 2D/3D

3D effects always play a role in the prediction of stall occurrence. However, in some cases, 2D computational results can be closer to experimental ones.

Comparison RANS/DES

3D RANS computations usually give results closer to the 2D RANS than the 3D DES calculations. Again, 3D RANS calculations can give results closer to the experimental ones than the 3D DES calculations.

Influence of Transition

The implementation of a transition model, as well as the type of transition model, modifies noticeably the stall characteristics. It is indeed an essential component of the computations as it directly affects separation and the subsequent stall.

8.3 Stall Region

Comparison 2D/3D

3D effects always play a role for stalled airfoil. In particular, it can usually be observed that oscillations associated to vortex shedding have higher amplitudes in the 2D computations than in 3D.

Comparison RANS/DES

3D RANS computations doesn't capture the full turbulent wake structure that develops after stall, however they usually give sensible results as far as averaged values are concerned.

Influence of Transition

Transition modelling is playing an important role for 2D RANS computations. It can induce unsteady effects for 3D DES computations which are not present in the fully turbulent case.

8.4 Deep Stall

Comparison 2D/3D

3D computations are necessary. 2D calculations usually become non-physical.

Comparison RANS/DES

The conclusions are the same as in the stall region. But again, usually the discrepancies observed between the mean values of lift and drag are not large. Discrepancies are mainly observed on the time-variations of these values.

Influence of Transition

Transition is not relevant as the flow is always completely detached on the suction side of the airfoil.

8.5 Summary

Several factors can play a role at the same time which can make it difficult to correctly analyze the results. Therefore, it is quite difficult to give general answers. Moreover, only four airfoils (even if representative of typical airfoil behaviors) have been studied.

One of the main conclusions of the study, even if already well-known, is the fact that transition is a major factor for the prediction of aerodynamic characteristics. In one case (for the NACA 63-430 airfoil), it is surmised that the transition model used in our computation is not suitable for comparison with the available experimental results. Indeed, in this case a by-pass transition model is probably needed (as indicated by 2D calculations in [13]). Another possible remedy might be the implementation of an actual 3D transition model, as the three-dimensionality of the flow might interact with transition location along the blade.

Another important conclusion is the fact that only 3D DES computations are able to reproduce the actual chaotic and three-dimensional of the turbulent wake in stall. This becomes relevant as far as one is interested in the unsteady aerodynamic loads that can be experienced by an airfoil.

Finally, it was observed in some cases that models that are expected to be more accurate (3D vs. 2D, DES vs. RANS) are not always giving the best results when compared to experimental ones. Several conclusions can be drawn from this fact. Firstly, the validity of the experimental data is always a subject of concern as there is never full control of all experimental and measurement conditions, as well as the several wind tunnel effects. Secondly, and which is more relevant for the present study, it is not always given beforehand that the use of a particular model is valid or justified. For example, 3D DES computations with a too coarse or too distorted computational grid, or a transition model ill-calibrated for the considered experiment, will most probably produce erroneous results.

9 Conclusion

A large number of numerical Navier-Stokes simulations involving two- and three-dimensional computations, RANS and DES modelling, fully turbulent computations or with transition model, have been performed. Four different airfoil profiles were considered. The results were compared and analyzed.

Several mechanisms explaining the discrepancies between the different numerical simulations, and some of the experimental results, have been identified. However, these conclusions cannot in general be applied to all types of airfoils. The two major conclusions of this work are the dependency of computational results to transition modelling, and the ability of 3D DES calculations to realistically simulate the turbulent wake of an airfoil in stall.

Acknowledgements

This work was carried out under a contract with The Danish Energy Authority, ENS-33031-0077, "Research Program in Applied Aeroelasticity (EFP-2005)". Computations were made possible by the use of the Linux cluster at the Risø central computing facility, and the computational resources of the Danish Center for Scientific Computing at MEK/DTU in Lyngby.

References

[1] Bertagnolio, F., Sørensen, N.N., Johansen, J. and Fuglsang, P., 2001, "Wind Turbine Airfoil Catalogue", Tech. Report Risø-R-1280(EN), Risø National Laboratory, Roskilde, Denmark.

[2] Bertagnolio, F., Sørensen, N.N. and Rasmussen, F., 2005, "New Insight Into the Flow Around a Wind Turbine Airfoil Section", J. Solar Energy Eng. (Trans. of ASME), Vol.127, pp.214-222.

[3] Bertagnolio, F., 2004, "Numerical Study of the Static and Pitching RISØ-B1-18 Airfoil", Tech. Report Risø-R-1448(EN), Risø National Laboratory, Roskilde, Denmark.

[4] Drela, M. and Giles, M. B., 1987, "Viscous-Inviscid Analysis of Transonic and Low Reynolds Number Airfoils", AIAA Journal, Vol.25, No.10, pp.1347-1355.

[5] Fuglsang, P., Antoniou, I., Dahl, K.S. and Madsen, H.Aa., 1998, "Wind Tunnel Tests of the FFA-W3-241, FFA-W3-301 and NACA 63-430 Airfoils", Tech. Report Risø-R-1041(EN), Risø National Laboratory, Roskilde, Denmark.

[6] Fuglsang, P., Antoniou, I., Sørensen, N.N. and Madsen, H.Aa., 1998, "Validation of a Wind Tunnel Testing Facility for Blade Surface Pressure Measurements", Tech. Report Risø-R-981(EN), Risø National Laboratory, Roskilde, Denmark.

[7] Fuglsang, P., Bak, C., Gaunaa, M. and Antoniou, I., 2003, "Wind Tunnel Tests of Risø-B1-18 and Risø-B1-24", Tech. Report Risø-R-1375(EN), Risø National Laboratory, Roskilde, Denmark.

[8] Issa, R.I., 1985, "Solution of the Implicitly Discretized Fluid Flow Equations by Operator-Splitting", J. Computational Physics, Vol.62, pp.40-65.

[9] Johansen, J., Sørensen, N.N., Michelsen, J.A. and Schreck, S., 2001, "Detached-Eddy Simulation of Flow around the S809 Airfoil", European Wind Energy Conference 2001, 2-6 July, Copenhagen, Denmark.

[10] Johansen, J., Srensen N.N., Michelsen, J.A. and Schreck, S., 2002, "Detached-Eddy Simulation of Flow around the NREL Phase-VI Blade", Wind Energy, Vol.5, pp.185-197.

[11] Leonard, B.P., 1979, "A Stable and Accurate Convective Modeling Procedure Based Upon Quadratic Upstream Interpolation", Comput. Methods Appl. Mech. Eng., Vol.19, pp.59-98.

[12] Menter, F.R., 1993, "Zonal Two-Equations $k-\omega$ Turbulence Models for Aerodynamic Flows", AIAA Paper 93-2906.

[13] Madsen, H.Aa. (ed.), 2002, Aeroelastic Research Program EFP-2001, Tech. Report Risø-R-1349(DA), Risø National Lab., Roskilde, Denmark (In danish).

[14] Michelsen, J.A., 1992, "Basis3D - A Platform for Development of Multiblock PDE Solvers", Tech. Report AFM 92-05, Technical University of Denmark, Lyngby, Denmark.

[15] Michelsen, J.A., 1994, "Block Structured Multigrid Solution of 2D and 3D Elliptic PDE's", Tech. Report AFM 94-06, Technical University of Denmark, Lyngby, Denmark.

[16] Rhie, C.M. and Chow, W.L., 1983, "Numerical Study of the Turbulent Flow Past an Airfoil with Trailing Edge Separation", AIAA Journal, Vol.21, pp.1525-1532.

[17] Sørensen, N.N., 1995, "General Purpose Flow Solver Applied to Flow over Hills", PhD Thesis, Tech. Report Risø-R-827(EN), Risø National Laboratory, Roskilde, Denmark.

[18] Sørensen, N.N., 2002, "Transition Prediction on the NORDTANK 500/41 Turbine Rotor", Tech. Report Risø-R-1365(EN), Risø National Lab., Roskilde, Denmark.

[19] Smagorinsky, J., 1963, "General Circulation Experiments with the Primitive Equations. I: The Basic Experiment", Month. Weath. Rev., Vol.91, No.3, pp.99-165.

[20] Somers, D.M., 1997, "Design and Experimental Results for the S809 Airfoil", Tech. Report NREL/SR-440-6918, National Renewable Energy Laboratory, Colorado, USA.

[21] Spalart, P.R., Jou, W-H., Strelets, M. and Allmaras, S.R., 1997, "Comments on the Feasibility of LES for Wings, and on a Hybrid RANS/LES Approach", Proc. of 1st AFOSR Int. Conf. on DNS/LES, Ruston, LA, August 4-8, Greyden Press, Columbus, OH.

[22] Strelets, M., 2001, "Detached Eddy Simulation of Massively Separated Flows", 39th AIAA Aerospace Sciences Meeting and Exhibit, AIAA Paper 2001-0879, Reno, NV.

[23] Timmer, W.A., 1992, "The Design and Testing of Airfoil DU 91-W2-250", 6th IEA Symposium on the Aerodynamics of Wind Turbines, Petten, The Netherlands.

[24] Timmer, W.A. and van Rooy, R.P.J.O.M., 1993, "Wind Tunnel Results for a 25% Thick Wind Turbine Blade Airfoil", European Community Wind Energy Conference, 8-12 March, Lübeck-Travemünde, Germany.

Risø's research is aimed at solving concrete problems in the society.

Research targets are set through continuous dialogue with business, the political system and researchers.

The effects of our research are sustainable energy supply and new technology for the health sector.